

**SP-1274**  
**June 2003**

**Images of the Solar Upper Atmosphere  
from SUMER on SOHO**

**Uri Feldman**

Artep Inc. 2922 Excelsior Spring Ct.  
Ellicott City, Maryland 21042, USA

and

E.O. Hulburt Center for Space Research,  
Naval Research Laboratory (NRL),  
Washington DC 20375-5352, USA

**Ingolf E. Dammasch** and **Klaus Wilhelm**

Max-Planck-Institut für Aeronomie (MPAE)  
37191 Katlenburg-Lindau, Germany

**Philippe Lemaire**

Institut d'Astrophysique Spatiale (IAS),  
Unité Mixte CNRS - Université Paris XI,  
91405 Orsay, France

**Donald M. Hassler**

Southwest Research Institute (SwRI),  
Boulder, CO 80302, USA

***European Space Agency***  
***Agence spatiale européenne***

**Cover:**

High-resolution images of a solar coronal hole obtained by SOHO's SUMER instrument on 28 and 29 July 1996. These observations in four spectral lines are representative of different temperature regimes in the solar atmosphere. The emission lines from top to bottom are:

- Fe XII with a wavelength of 1241.990 Å and a formation temperature of  $1.4 \times 10^6$  K
- Mg X with a wavelength of 624.965 Å and a formation temperature of  $1.1 \times 10^6$  K
- N V with a wavelength of 1238.821 Å and a formation temperature of  $1.9 \times 10^5$  K, and
- C I with a wavelength of 1249.405 Å and a formation temperature of just over  $1.3 \times 10^4$  K.

The C I image shows the chromospheric network. Spicules and a pronounced limb brightening can be seen in N V. The Mg X exposure highlights the polar plumes and coronal bright points, whereas the Fe XII image outlines the coronal hole and its boundaries. (The displays of the solar south pole are inverted for graphical reasons.)

<i>Published by</i>	ESA Publications Division ESTEC, PO Box 299, 2200 AG Noordwijk, The Netherlands
<i>Editor</i>	Bruce Battick
<i>Layout</i>	Paul Berkhout
<i>Printed in</i>	The Netherlands
<i>Price</i>	50 Euros
<i>ISBN</i>	92-9092-981-2
<i>ISSN</i>	0379-6566
<i>Copyright</i>	© 2003 European Space Agency

# Contents

<b>Preface</b>	<b>ii</b>
<b>Abbreviations</b>	<b>iii</b>
<b>Acknowledgements</b>	<b>iv</b>
<b>1 Introduction</b>	<b>1</b>
1.1 Scientific Background . . . . .	1
1.2 The <i>SOHO</i> Mission . . . . .	2
1.3 The SUMER Instrument . . . . .	2
1.4 Solar Observations . . . . .	3
<b>2 Technical Description of SUMER</b>	<b>5</b>
2.1 Concepts . . . . .	5
2.2 The Telescope . . . . .	6
2.3 The Rear Slit Camera . . . . .	6
2.4 The Spectrograph . . . . .	6
2.5 The Detectors . . . . .	6
2.6 The Electronics . . . . .	6
2.7 Software and SUMER Command Language . . . . .	7
2.8 Radiometric Ground Calibration . . . . .	7
<b>3 Performance during Solar Observations</b>	<b>8</b>
3.1 Spatial Resolution . . . . .	8
3.2 Spectral Resolution . . . . .	8
3.3 Thermal Stability . . . . .	8
3.4 Inflight Radiometric Calibration . . . . .	9
<b>4 Image Processing</b>	<b>12</b>
<b>5 Description of Images</b>	<b>14</b>
5.1 General Considerations . . . . .	14
5.2 Full-Sun Images at Highest Spatial Resolution . . . . .	15
5.3 Full-Sun Images with Reduced Resolution . . . . .	17
5.4 Synoptic Studies of the Sun in HI and SVI . . . . .	18
5.5 Whole-Sun Month Observations . . . . .	19
5.6 Equatorial Radiance Variations . . . . .	22
5.7 Emission-line and Spectral Irradiances . . . . .	24
<b>6 Summary</b>	<b>26</b>
<b>Bibliography</b>	<b>27</b>
<b>The Atlas of SUMER Images</b>	<b>31</b>

# Preface

Investigations of the heating of the corona and the acceleration of the solar wind are two of the prime scientific goals in studying the solar upper atmosphere with the *Solar and Heliospheric Observatory (SOHO)* of ESA and NASA. The telescope and spectrometer Solar Ultraviolet Measurements of Emitted Radiation (SUMER), one of the twelve scientific instruments aboard *SOHO*, was designed for spectroscopic studies of the solar chromosphere, transition region, and low corona with emphasis on the dynamics in these regions. However, the imaging capabilities of SUMER also led to a wealth of observations on the morphology of the solar atmosphere. The aim of this publication is to present these images in a systematic way – without a detailed scientific evaluation – in atlas form. All images were obtained by a scanning process of the SUMER slit spectrograph across the solar disk and its near environment. This volume contains most of the full-Sun images exposed by SUMER during the *SOHO* mission, and the coronal-hole observations obtained by this instrument during the “Whole-Sun Month” in August and September 1996. In addition, it provides an overview of the SUMER project. Additional partial images of large and small areas of the Sun are available, but are not included in this volume.

The SUMER instrument has been proposed, developed and operated by the SUMER Investigators:

K. Wilhelm, MPAE<sup>1</sup>, Germany (PI until 28 February 2002); P. Lemaire, IAS, France; W. Curdt, MPAE, Germany (PI since 1 March 2002); U. Schühle, MPAE, Germany; E. Marsch, MPAE, Germany; A.I. Poland, GSFC, USA; S.D. Jordan, GSFC, USA; R.J. Thomas, GSFC, USA; D.M. Hassler, HAO (now at SwRI), USA; M.C.E. Huber, SSD/ESTEC, The Netherlands; J.-C. Vial, IAS, France; M. Kühne, PTB, Germany; O.H.W. Siegmund, SSL, USA; A.H. Gabriel, IAS, France; J.G. Timothy, CSSA (now at Nightsen), USA; and M. Grewing, AIT, Germany.

Scientific advice during all phases of the project has been provided by a group of Associated Scientists:

J. Aboudarham, B. Aschenbach, W.I. Axford, J. Barnstedt, F. Bely-Dubau, K. Bocchialini, V. Bommier, P. Brekke, N. Brynildsen, M. Carlsson, J. Chae, J.L. Culhane, I.E. Dammasch, C.R. de Boer, J.P. Delaboudinière, C. Diesch, G.A. Doschek, J.G. Doyle, J. Dubau, B.N. Dwivedi, G. Einaudi, U. Feldman, A. Fludra, B.H. Foing, P. Gouttebroze, V.H. Hansteen, R.A. Harrison, E. Haug, H.F. Haupt, P. Heinzel, J. Hollandt, D.E. Innes, W.-H. Ip, C. Jordan, P.G. Judge, F.P. Keenan, O. Kjeldseth-Moe, B. Kliem, F. Kneer, T.A. Kucera, J.M. Laming, J. Lang, K.R. Lang, B. Leroy, O. von der Lühe, P. Maltby, J.T. Mariska, M. Mathioudakis, T.G. Moran, H.E. Mason, R.W.P. McWhirter, P. Mein, F. Millier, K. Norman, J.H. Parkinson, H. Peter, E.R. Priest, A.K. Richter, H. Rosenbauer, S. Sahal, D. Samain, B. Schmieder, J.H.M.M. Schmitt, M. Schüssler, R. Schwenn, G.M. Simnett, W.T. Thompson, G. Tondello, J. Trümper, V.M. Vasyliunas, O. Vilhu, and H.P. Warren.

The design, development, qualification, and operation of the SUMER instrument have been carried out or supported by an Engineering and Management Team:

A. Arondel, S.J. Battel, L. Bemann, H.-M. Bock, R. Bodmer, R. Boucarut, P. Boutry, P. Bouyries, H.-J. Braun, I. Büttner, A. Dannenberg, W. Donakowski, D. Dumont, M.L. Edgar, W. Engelhardt, H.-G. Engelmann, K. Eulig, P. Fahlbusch, A. Fischer, E. Frank, G.A. Gaines, D. Germerott, D. Gigas, K. Gräbig, W. Grill, M.A. Gummin, J.W. Hamilton, H. Hartwig, E. Hertzberg, J. Hoberman, G. Hoch, J. Hollis, J. Hull, P.N. Jelinsky, S.R. Jelinsky, P. Jensen, M.D. Jhabvala, H.G. Kellner, K. Kellner, E. Keppler, R.A. Keski-Kuha, E. Korzac, K. Lattner, D.B. Levinton, J. Linant, Y. Longval, T. Magoncelli, C. Maroney, C. Maurel, R. Meller, N. Morisset, N. Mosquet, N. Neisen, C. Neu, W. Neumann, J.F. Osantowski, I. Pardowitz, A. Pauly, W. Paustian, E. Petit, J. Platzer, K. Poser, R. Raffanti, W. Reich, T. Rodriguez-Bell, T.T. Saha, T.P. Sasseen, H. Schild, R. Schmidt, H. Schüddekopf, I. Schwarz, H. Specht, E. Steinmetz, J.M. Stock, U. Strohmeyer, W. Tappert, S. Töpfer, J.L. Tom, G. Tomasch, J.V. Vallerga, B. Wand, L. Wang, B.Y. Welsh, and G. Wright.

The work of many industrial contractors was essential in designing and manufacturing most of the sub-systems of SUMER and its flight and ground software.

During the operational phase, SUMER observations<sup>2</sup> have been obtained by members of the core teams listed above as Weekly Planners, a task that was also performed by:

T.A. Ayres, K.P. Dere, G.H. Fisher, E. Landi, D.W. Longcope, K. Muglach, F. Paletou, I. Rüedi, and J.F. Seely.

---

<sup>1</sup>The full names of the affiliations are included in the list of abbreviations.

<sup>2</sup>All SUMER data acquired in the public domain and can be obtained from the SOHO Archive (<http://soho.nascom.nasa.gov/data/catalogues/main.html>) or from the SUMER Image Database (<http://www.linmpi.mpg.de/english/projekte/sumer/FILE/SumerEntryPage.html>).

# Abbreviations

AIT – Astronomisches Institut Tübingen  
BESSY I – Berlin Electron Storage ring for SYNchrotron radiation  
CDS – Coronal Diagnostic Spectrometer  
CH – Coronal Hole  
CNES – Centre National d’Etudes Spatiales  
CSSA – Center for Space Science and Astrophysics  
CVD SiC – Chemical-Vapour Deposited SiC  
DLR – Deutsches Zentrum für Luft- und Raumfahrt  
DPU – Data Processing Unit  
DSN – Deep Space Network  
EIT – Extreme-ultraviolet Imaging Telescope  
EOF – Experimenters’ Operations Facility  
ESA – European Space Agency  
ESTEC – European Space Technology Centre  
EUV – Extreme Ultraviolet  
FIP – First-Ionization Potential  
FWHM – Full-Width at Half Maximum  
GSFC – Goddard Space Flight Center/NASA  
HAO – High Altitude Observatory  
HULLAC – Hebrew University Lawrence Livermore Atomic Code  
IAS – Institut d’Astrophysique Spatiale  
IIM – Image Integration Memory  
*IUE – International Ultraviolet Explorer*  
JOP – Joint Observational Programme  
LASCO – Large Angle Spectroscopic Coronagraph  
MCP – Micro-Channel Plate  
MDI – Michelson Doppler Imager  
MPAE – Max-Planck-Institut für Aeronomie  
MPG – Max-Planck-Gesellschaft  
NASA – National Aeronautics and Space Administration  
NGDC – National Geophysical Data Center  
NRL – Naval Research Laboratory  
PI – Principal Investigator  
POP – Pre-defined Observational Programme  
PRODEX – Programme de Développement d’Expériences Scientifiques  
PSF – Point Spread Function  
PTB – Physikalisch-Technische Bundesanstalt  
RSC – Rear Slit Camera  
SCL – SUMER Command Language  
*SOHO – Solar and Heliospheric Observatory*  
SOLSTICE – SOLAR-STellar Irradiance Comparison Experiment  
SSD – Space Science Department/ESTEC  
SSL – Space Science Laboratory  
SUMER – Solar Ultraviolet Measurements of Emitted Radiation  
SUPERACO – SUPER Anneau de Collisions d’Orsay  
SwRI – Southwest Research Institute  
*UARS – Upper Atmosphere Research Satellite*  
UDP – User-Defined Programme  
UTC – Coordinated Universal Time  
UVCS – Ultraviolet Coronagraph Spectrometer  
XDL – Cross Delay Line.

# Acknowledgements

The SUMER project is financed by the Deutsches Zentrum für Luft- und Raumfahrt (DLR), the Centre National d'Etudes Spatiales (CNES), the National Aeronautics and Space Administration (NASA), the European Space Agency's (ESA) PRODEX programme (Swiss contribution), and by the Max-Planck-Gesellschaft (MPG). We acknowledge the contributions of our late colleagues C. Becker, I. Liede, B. Monsignori-Fossi and B.E. Patchett. The instrument is part of the *SOHO* payload. All solar images presented in this atlas were obtained before the accidental attitude loss of *SOHO*, but we nevertheless want to acknowledge the extraordinary performance of the *SOHO* Recovery Team led by F.C. Vandenbussche in 1998. Although *SOHO* had completed its nominal mission at that time, the additional observations made possible after the recovery in the years of the sunspot maximum are invaluable, and especially can be compared with the solar atmosphere during the minimum of the solar activity shown here. We are grateful to B. Fleck for his encouragement during the planning phase of the SUMER atlas of solar images, to B.N. Dwivedi for a critical review of the manuscript, to ESA for funding its publication, and to B. Battick and P. Berkhout of the ESA Publications Division for their support during the publication process.

# Chapter 1

## Introduction

### 1.1 Scientific Background

The solar upper atmosphere is defined as the region spanning the range from  $T_e = 1 \times 10^4$  K to  $3 \times 10^7$  K in electron temperature. This region is composed of structures of different shapes, sizes, temperatures and lifetimes, and is in a constant state of change. In order to understand fully the properties of these structures and the means by which they are maintained, high-resolution monochromatic images are needed covering the entire temperature domain of the solar upper atmosphere. To image plasma within a narrow temperature range, it is required to detect emission from a single line formed in the range of interest. Unfortunately, most of the solar spectral regions are crowded with lines that are emitted by plasmas of different temperatures. A review of solar ultraviolet observations with emphasis on spectral line identifications has recently been published by Wilhelm (2003).

A spectroheliograph was the first instrument that succeeded in recording high-resolution monochromatic solar images (Zirin, 1966). Its original design incorporated a telescope and a spectrograph that operated as a monochromator, i.e. in addition to an entrance slit, the spectrograph contained a movable slit that could be tuned to a desired wavelength. The alignment between the two instruments was such that the entrance slit of the spectrograph was placed at the focal plane of the telescope. By moving the solar image across the slit of the spectrograph and by synchronizing this motion with the movement across the exit slit of a photographic plate an image of the Sun in a single spectral line could be produced. Such a spectroheliograph turned out to be a very efficient, although slow, instrument for recording images of the solar atmosphere at any wavelength within its operational range.

The time required to record a solar image could obviously be reduced significantly by replacing the high-resolution spectrograph with a narrow-band filter that is capable of transmitting a selected spectral line or a group of lines while blocking the rest. An instrument that comes close to fulfilling this imaging requirement is a telescope equipped with a high-quality birefringent filter (Evans, 1953). These devices are very efficient at wavelengths that are not absorbed by the filter components. Unfortunately, the bright spectral lines emitted by the solar plasma have wavelengths with  $\lambda \leq 1600$  Å and thus are absorbed by such filters.

Despite the many emission lines of the solar spectrum, there are several spectral windows, mostly in the extreme ultraviolet (EUV), where, under normal solar conditions, one or two bright lines dominate the emission in a narrow wavelength range ( $\Delta\lambda/\lambda \approx 1/20$ ). The most prominent among these are the 304 Å band dominated by the He II resonance lines, the 174 Å band dominated by Fe IX and Fe X lines, the 192 Å band dominated by Fe XII lines, and the 284 Å band dominated by a Fe XV line. These spectral windows can be observed with the help of multilayer optics (Walker et al., 1988). The iron bands in general are fairly adequate for imaging solar plasmas in the  $8 \times 10^5$  K  $\leq T_e \leq 2 \times 10^6$  K range, whereas the 304 Å band is used to image  $8 \times 10^4$  K solar plasmas. Due to the finite widths of the wavelength pass bands, the solar images obtained with telescopes equipped with multilayer mirrors are also not free from problems. This is because lines and free-free emission, which are emitted by other temperature regimes and are suppressed under normal conditions, can become quite strong in many cases. Examples are the Si XI resonance line in the 304 Å band, or the Fe XXIV and Ca XVII resonance lines in the 192 Å band, which become increasingly more intense as the solar activity increases.

At the short end of the spectrum, the spectral lines are generally ordered according to their formation temperature (defined in Section 1.4). As the temperatures of the plasma increase, the wavelengths of the emitted lines in general become shorter and shift towards the X-ray regime. Grazing-incidence telescopes equipped with several filters, each transmitting a slightly different pass band, are frequently used to image the very hot coronal plasmas of the Sun with  $T_e \geq 2 \times 10^6$  K.

Techniques employing narrow-band filters, however, fail to generate images with the desired spectroscopic quality that are needed to reveal the morphological properties of solar upper atmosphere and, in particular, those in the range of  $T_e = 2 \times 10^4$  K to  $7 \times 10^5$  K. SUMER is the first instrument that succeeded in imaging this important domain in detail. As with a traditional spectroheliograph, images could be produced with a very high spectral purity at many wavelengths although at a fairly slow cadence.

## 1.2 The *SOHO* Mission

*SOHO* is dedicated to furthering our understanding of the solar interior, the solar atmosphere and the solar wind. To accomplish these goals, the spacecraft carries a set of twelve instruments designed to make measurements throughout the electromagnetic spectrum, as well as detecting solar particles at all energies. The *SOHO* payload contains several instruments to measure surface oscillations using the Doppler effect as well as irradiance or radiance changes. These observations must be made during long uninterrupted time intervals; this requirement is met by placing the spacecraft at the inner Sun-Earth Lagrange point (L1), where the gravitational forces of the Sun and the Earth together with the centrifugal force cancel each other. All other *SOHO* instruments also benefit from such a continuous view of the Sun. The *SOHO* spacecraft shown in Figure 1.1 consists of a payload module accommodating the scientific instruments, and a service module carrying the spacecraft systems and the solar arrays. It is stabilized in three axes and is pointed towards the Sun with an accuracy of better than  $1''$  in time intervals of 15 min ( $1'' \approx 4.85 \times 10^{-6}$  rad corresponds to approximately 715 km on the Sun).

*SOHO* was launched on 2 December 1995 and was injected into a halo orbit around L1, about  $1.5 \times 10^6$  km sunwards from the Earth in early 1996. This orbit has a period of  $\approx 180$  d. Although *SOHO* was designed for a lifetime of two years, an extension of several years is still in progress at the time of writing this report. The spacecraft flight operations support activities are centred at the NASA Goddard Space Flight Center (GSFC). Contact with the spacecraft is achieved by using the Deep Space Network (DSN). Data are transmitted in real time to the ground or to the spacecraft tape recorder, which is played back at the start of contact periods. The data are passed to the Experimenters' Operations Facility (EOF). The payload instruments are controlled by the experiment teams and allow interactive as well as routine operations to be carried out in near-real time (cf. Fleck et al., 1995; St.Cyr et al., 1995; Fleck and Švestka, 1997).

## 1.3 The SUMER Instrument

The SUMER instrument is capable of recording high-resolution spectra of lines and the continua in the  $465 \text{ \AA}$  to  $1610 \text{ \AA}$  wavelength range ( $1 \text{ \AA} = 0.1 \text{ nm}$ ). It is primarily a high-resolution stigmatic slit spectrograph (for a technical description see Chapter 2), but is also equipped with sophisticated imaging capabilities. In order to obtain an image of the solar disk at a particular wavelength, the image of the Sun is stepped with the help of a telescope mechanism across the slit in the east-west or west-east direction while one of the two-dimensional detectors records the spectral radiance in the desired wavelength range. With *SOHO* in its nominal attitude, the SUMER instrument is oriented such that its slit, which can be selected from a set of four, is aligned along the solar north-south direction, but during *SOHO* roll manoeuvres, which were carried out from time to time, other orientations have been attained (cf. Dammasch et al., 1999a).

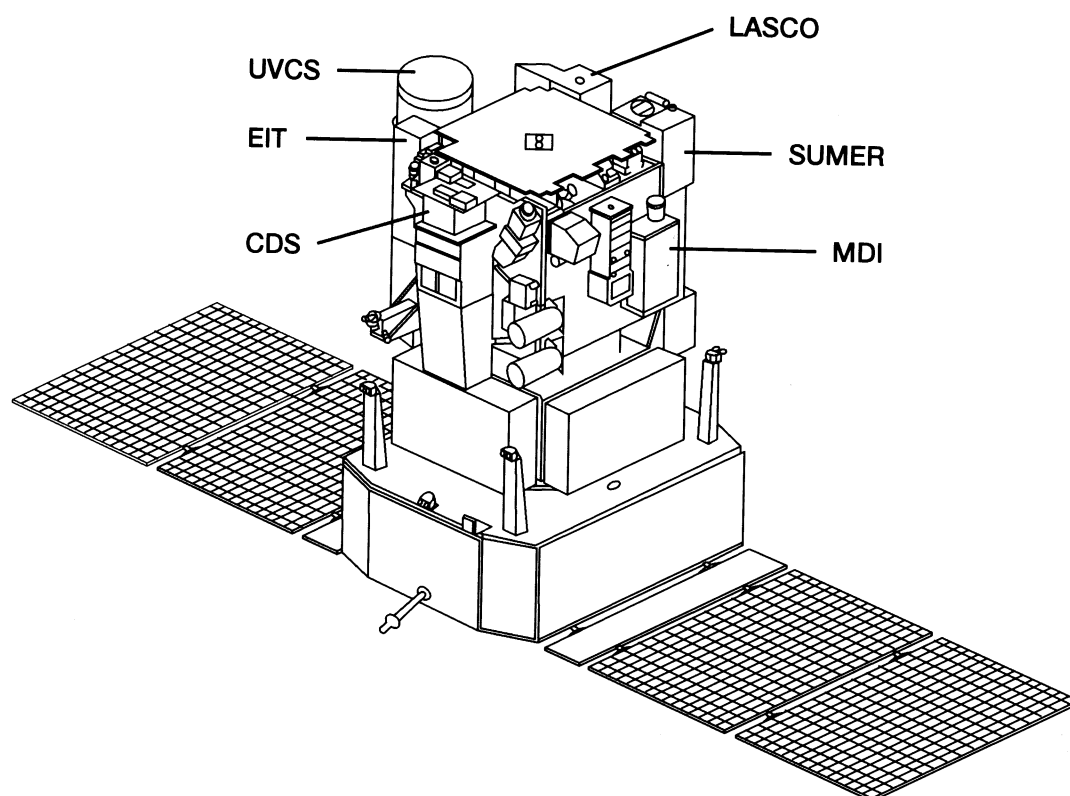


Figure 1.1: A drawing of the *SOHO* spacecraft showing the service and the payload modules with the locations of the scientific instruments mentioned in this atlas. The spacecraft is stabilized in three axes and is permanently pointing to the centre of the solar disk.

As the solar image is moved relative to the slit from limb to limb in the east-west direction a slice of the solar disk is imaged corresponding to the length of the slit. When such a scan is completed, the solar image can be raised or lowered to the proper distance in the north-south direction by a second telescope mechanism, before another east-west scan is executed. Since the solar disk as seen from *SOHO* corresponds to approximately three million seconds of arc squared and the  $1'' \times 300''$  wide slit covers only three hundred seconds of arc squared at any one instant, a minimum of  $10^4$  steps are needed to produce a full-resolution Sun image. Depending on the integration time at each step, it may take several hours to more than a day to record such an image.

These unique imaging capabilities, for the first time, revealed morphological details of the quiet-Sun, coronal-hole, and, to a lesser extent, active-region plasmas ranging in electron temperatures from  $T_e \approx 1 \times 10^4$  K (continuum, Si I line) to  $T_e \approx 1.4 \times 10^6$  K (Fe XII line) (cf. Table 1.1).

## 1.4 Solar Observations

This atlas of SUMER images is the first collection ever published of solar upper-atmosphere images in spectral lines or continuum radiation, at spatial resolutions approaching  $1''$ , that spans the temperature range from the chromosphere to the corona. Most of the images presented in this volume were recorded in radiation emitted by the brightest lines in the 465 Å to 1610 Å SUMER range. For a list of lines observed by SUMER on the solar disk and the corona see Curdt et al. (1997, 2001) and Feldman et al. (1997). Table 1.1 summarizes some of the properties of the spectral lines in which the images were obtained, and Figure 1.2 displays in the upper panel (a) the ionic fractions of the radiating ions, and in the lower panel (b) the normalized contribution functions versus the electron temperature under ionization equilibrium conditions. The temperature at which a contribution function peaks is usually referred to as the formation temperature,  $T_F$ , of a spectral line.

Since the images presented in the atlas were recorded during 1996, when the solar magnetic activity cycle was at minimum, most of the solar surface during the observations was covered by quiet-Sun and coronal-hole regions, but some of the images also include weak centres of activity. Interestingly, although the areas of activity, when present, were small, their effect on surrounding regions was profound.

The programme that generated the full-Sun images was initialized by aligning the telescope mirror to an off-limb south-east region. With the  $1'' \times 300''$  slit in place, the spectrometer optics were adjusted such that the spectral information from a desired wavelength band would be imaged on the detector. A  $300''$  wide strip was then rastered by moving the solar image across the aperture in equal step sizes and integration times along the east-west direction. At the completion of the first raster the solar image was shifted in the north-south direction by  $\approx 270''$  and a second strip was rastered in reversed direction. The procedure was repeated eight times until the entire solar area was imaged in

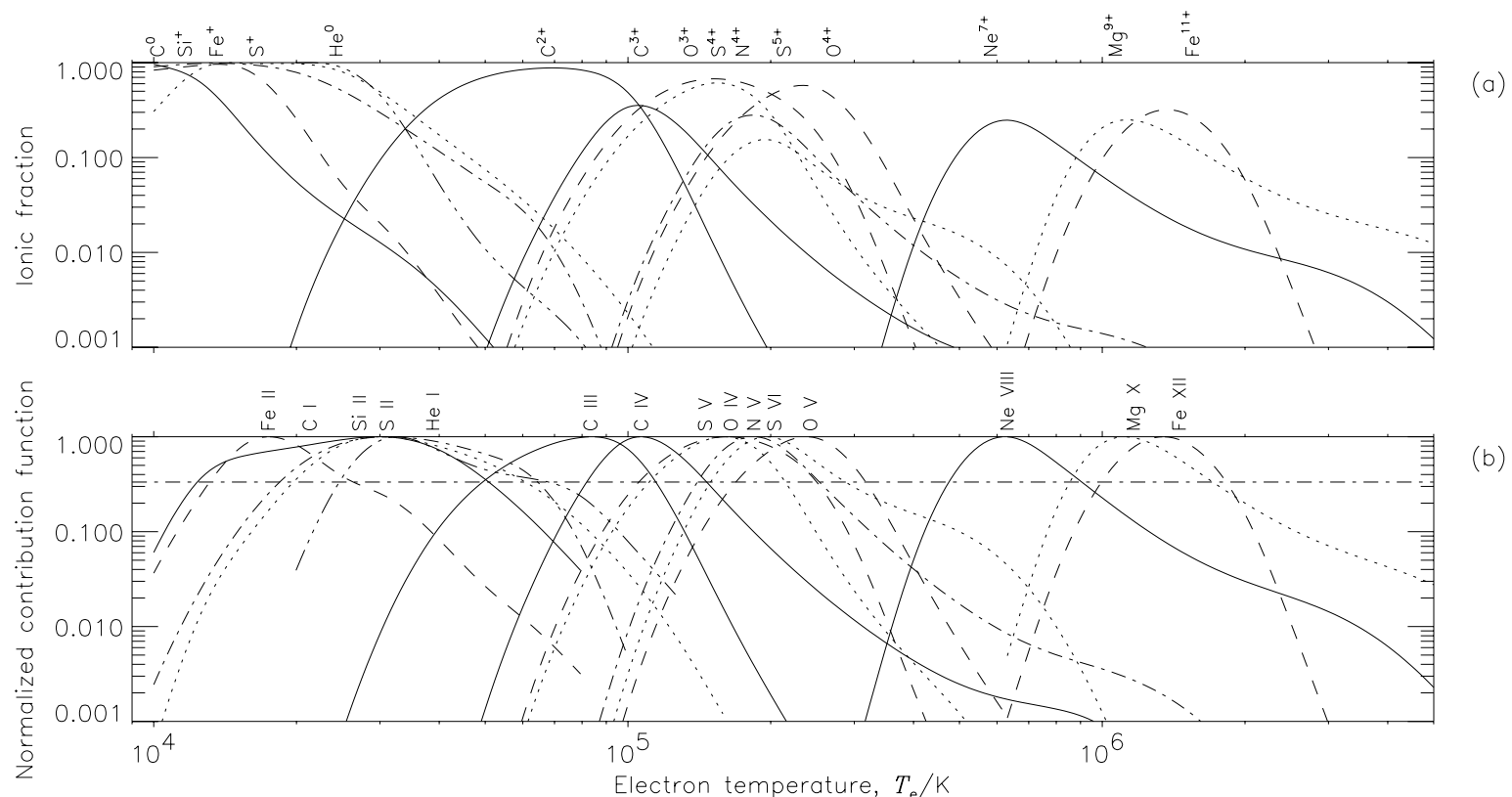


Figure 1.2: (a) Ionic fractions (after Mazzotta et al., 1998) and (b) normalized contribution functions of relevant emission lines (except H I and Si I). Note the long high-temperature tails of the Li-like ions  $C^{3+}$ ,  $N^{4+}$ ,  $Ne^{7+}$ , and  $Mg^{9+}$ . The dashed-dotted horizontal line at one third was used to define the contribution temperatures in Table 1.1 (cf. Feldman, Dammasch & Wilhelm, 2000).

Table 1.1: A list of emission lines and continua with wavelengths, atoms or ions, spectroscopic designations and contribution temperatures related to the images displayed in this atlas. The formation temperatures of the lines increase from top to bottom.

Line, continuum	Wavelength <sup>a</sup> , $\lambda/\text{\AA}$	Species	Spectroscopic designation	Temperature <sup>b</sup> , $T_c/\text{K}, T_B/\text{K}$	Formation temperature, $T_F/\text{K}$
Continuum	1549	$\text{H}^0 + \text{Bb}^c$		$\approx 4500$	
Continuum	1241	$\text{Si}^0 + \text{Bb}^d$		$\approx 4700$	
Continuum	1169	$\text{S}^0 (+\text{Bb}^e)$		$\approx 5000$	
Continuum	812 <sup>f</sup>	$\text{H}^0$		$\approx 6700$	
Si I	1256.490	$\text{Si}^0$	$3s^2 3p^2 \ ^3P_1 - 3s 3p^3 \ ^3S_1$		$\approx 1.0 \times 10^4$
Fe II	1559.085	$\text{Fe}^+$	$3d^7 \ ^4F_{9/2} - 3d^6 4p \ ^4F_{9/2}$	$(1.3 \text{ to } 2.6) \times 10^4$	$1.7 \times 10^4$
H I	937.803	$\text{H}^0$	$1s \ ^2S_{1/2} - 6p \ ^2P_{1/2,3/2}$	$(1.3 \text{ to } 2.7) \times 10^4$	$1.8 \times 10^4$
C I	1249.405	$\text{C}^0$	$2s^2 2p^2 \ ^1D_2 - 2s^2 2p 3d \ ^1F_3$	$(1.3 \text{ to } 5.0) \times 10^4$	$3.0 \times 10^4$
S II	1250.578 <sup>g</sup>	$\text{S}^+$	$3s^2 3p^3 \ ^4S_{3/2} - 3s 3p^4 \ ^4P_{1/2}$	$(2.0 \text{ to } 6.0) \times 10^4$	$3.0 \times 10^4$
Si II	1250.433	$\text{Si}^+$	$3s 3p^2 \ ^2D_{5/2} - 3p^3 \ ^2D_{5/2}$	$(1.9 \text{ to } 6.3) \times 10^4$	$3.1 \times 10^4$
He I	584.334	$\text{He}^0$	$1s^2 \ ^1S_0 - 1s 2p \ ^1P_1$	$(2.5 \text{ to } 5.5) \times 10^4$	$3.2 \times 10^4$
C III	977.020	$\text{C}^{2+}$	$2s^2 \ ^1S_0 - 2s 2p \ ^1P_1$	$(0.5 \text{ to } 1.1) \times 10^5$	$8.3 \times 10^4$
C IV	1548.202	$\text{C}^{3+}$	$2s \ ^2S_{1/2} - 2p \ ^2P_{3/2}$	$(0.8 \text{ to } 1.4) \times 10^5$	$1.1 \times 10^5$
S V	786.48	$\text{S}^{4+}$	$3s^2 \ ^1S_0 - 3s 3p \ ^1P_1$	$(1.1 \text{ to } 2.1) \times 10^5$	$1.6 \times 10^5$
O IV	787.711	$\text{O}^{3+}$	$2s^2 2p \ ^2P_{1/2} - 2s 2p^2 \ ^2D_{3/2}$	$(1.1 \text{ to } 2.5) \times 10^5$	$1.6 \times 10^5$
O IV	790.199	$\text{O}^{3+}$	$2s^2 2p \ ^2P_{3/2} - 2s 2p^2 \ ^2D_{5/2}$	$(1.1 \text{ to } 2.5) \times 10^5$	$1.6 \times 10^5$
N V	1238.821	$\text{N}^{4+}$	$2s \ ^2S_{1/2} - 2p \ ^2P_{3/2}$	$(1.4 \text{ to } 2.5) \times 10^5$	$1.9 \times 10^5$
S VI	933.38	$\text{S}^{5+}$	$3s \ ^2S_{1/2} - 3p \ ^2P_{3/2}$	$(1.5 \text{ to } 2.8) \times 10^5$	$2.0 \times 10^5$
S VI	944.52	$\text{S}^{5+}$	$3s \ ^2S_{1/2} - 3p \ ^2P_{1/2}$	$(1.5 \text{ to } 2.8) \times 10^5$	$2.0 \times 10^5$
O V	629.730	$\text{O}^{4+}$	$2s^2 \ ^1S_0 - 2s 2p \ ^1P_1$	$(1.7 \text{ to } 3.2) \times 10^5$	$2.4 \times 10^5$
Ne VIII	770.428 <sup>h</sup>	$\text{Ne}^{7+}$	$2s \ ^2S_{1/2} - 2p \ ^2P_{3/2}$	$(4.8 \text{ to } 8.9) \times 10^5$	$6.2 \times 10^5$
Mg X	624.965 <sup>i</sup>	$\text{Mg}^{9+}$	$2s \ ^2S_{1/2} - 2p \ ^2P_{1/2}$	$(0.9 \text{ to } 1.7) \times 10^6$	$1.1 \times 10^6$
Fe XII	1241.990 <sup>i</sup>	$\text{Fe}^{11+}$	$3s^2 3p^3 \ ^4S_{3/2} - 3s^2 3p^3 \ ^2P_{3/2}$	$(1.0 \text{ to } 1.8) \times 10^6$	$1.4 \times 10^6$

<sup>a</sup> After Kelly (1987) unless indicated differently. The wavelengths will be given in round numbers in the remainder of the text.

<sup>b</sup> The contribution and formation temperatures of the lines have been obtained from Figure 1.2 (except for H I and Si I, which require a special treatment). The data for the atomic lines have to be considered as rough estimates, in particular in optically thick cases. The continuum entries refer to brightness temperatures.

<sup>c</sup> The radiation in this band is composed of the 1550 Å photospheric continuum (black body: Bb) and the second order 775 Å H I free-bound Lyman continuum.

<sup>d</sup> This radiation is composed of the 1241 Å photospheric continuum and the Si I free-bound continuum.

<sup>e</sup> Although some photospheric continuum may be present, most of the contribution comes from the S I continuum.

<sup>f</sup> The radiation in this band is dominated by the H I free-bound Lyman continuum.

<sup>g</sup> After Pettersen (1983).

<sup>h</sup> After Dammasch et al. (1999b).

<sup>i</sup> After Dammasch et al. (1999c).

this boustropheidon manner. The individual rastered strips were arranged such that overlapped regions of  $\approx 30''$  were obtained in adjacent sections. On 2 March and 26 June 1996, the He I images were recorded with a slightly modified observing programme.

Almost all full-disk images were taken on detector A. The only exceptions are the H I Ly $\epsilon$  and S VI images recorded between 24 September and 5 October (see Table 5.4) that were imaged on detector B. All images at wavelengths shorter than 790 Å were recorded in second order of the grating diffraction. An orthogonal coordinate system centred on the solar disk was used with  $+x$  in the west direction and  $+y$  directed towards north.

## Chapter 2

# Technical Description of SUMER

### 2.1 Concepts

The SUMER optical elements are made of silicon carbide (SiC) substrates with a polished coating of chemical vapour deposited (CVD) SiC, which is a fairly good reflector for radiation with wavelengths between 500 Å to 2000 Å. From the optical diagram of SUMER in Figure 2.1, it can be seen that each photon recorded by SUMER is reflected by three normal-incidence (telescope, collimator, and grating) and one grazing-incidence (plane scan mirror) SiC surfaces before reaching the detector. As the wavelength of the radiation approaches 500 Å from the long-wavelength side, the reflective properties of the SUMER optics rapidly decrease. Thus, only a few of the brightest lines with wavelengths shorter than 500 Å are visible in second order. The third-order responsivity of the SUMER grating is comparable to that of the second-order responsivity. As a result, about half a dozen third-order lines are also present.

Each step can be any multiple of the basic increment of  $0.375''$ . The integration time at each step is typically a few seconds to a few tens of seconds. Rastering can be executed in two different ways: (a) the slit moves to the new position in one step (normal step mode), or (b) is shifted in increments of  $0.375''$  across the selected step width with fractional sampling times at the intermediate positions (smear-step mode). All images in this atlas except the images of January 1996 (C III) in Section 5.2 and those of the Whole-Sun Month described in Section 5.5 have been exposed in smear-step

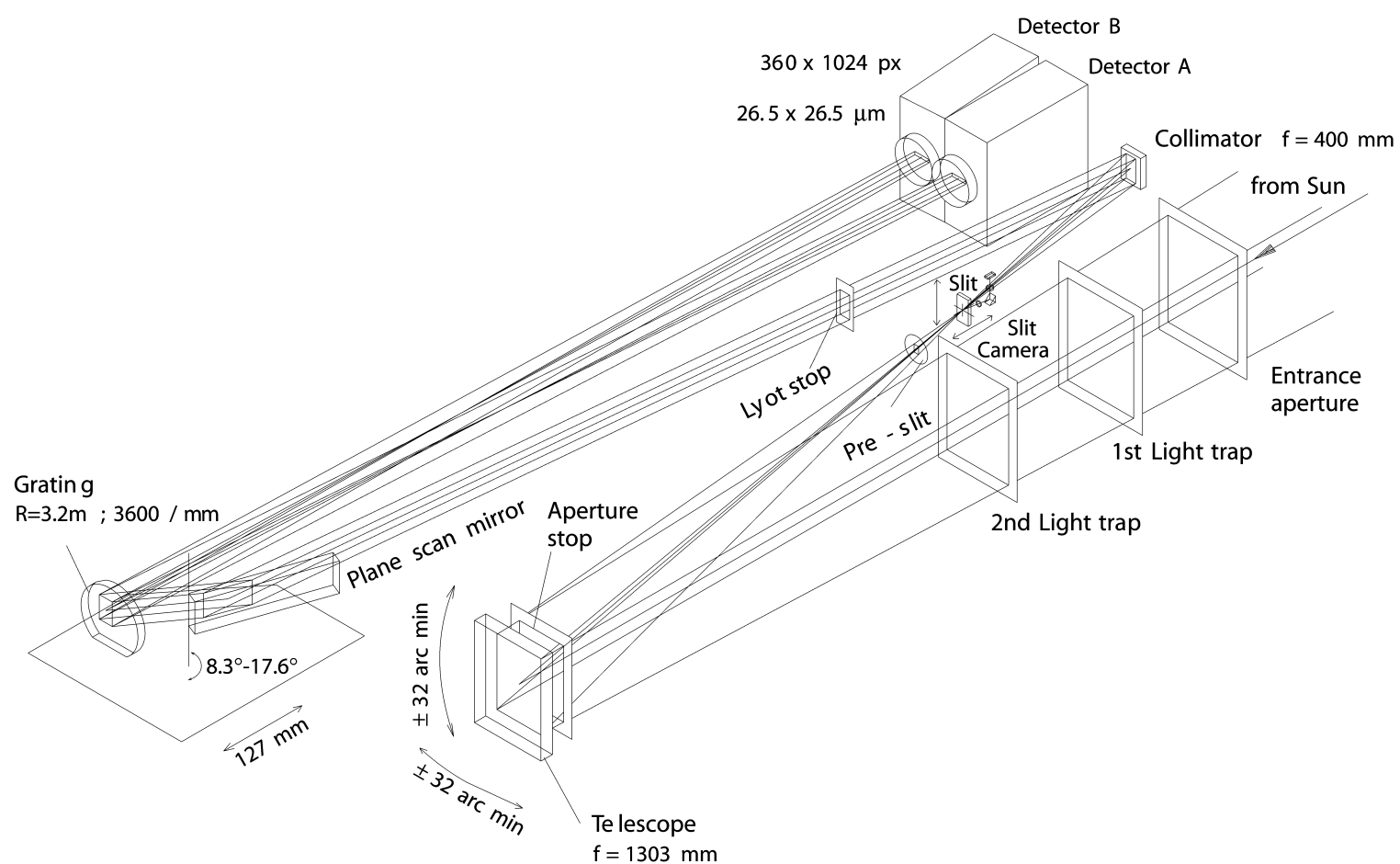


Figure 2.1: Optical diagram of SUMER. The structural elements of the optical bench, which also provide both cleanliness protection and thermal control functions, are not shown.

mode. Further details of the SUMER instrument and its modes of operation are described by Wilhelm et al. (1995a, b). In two later papers, accounts of the actual performance of SUMER under operational conditions are provided (Wilhelm et al., 1997a; Lemaire et al., 1997).

## 2.2 The Telescope

The telescope mirror is an off-axis paraboloid, which can image any area within a total dynamic field of view of  $64' \times 64'$  around the Sun on the spectrograph entrance slit. (The mean angular solar diameter as seen from *SOHO* is  $\approx 32'$ .) Some important telescope parameters are: a focal length of 1302.77 mm, an aperture stop area of  $9 \text{ cm} \times 13 \text{ cm}$ , an equivalent f-number of 10.67, and a plate scale in the slit plane of  $6.315 \mu\text{m}/''$ .

## 2.3 The Rear Slit Camera

The Rear Slit Camera (RSC) monitors the slit image in the diffracted beam of the visible portion of the solar spectrum (near  $6000 \text{ \AA}$ ). Although an internal alignment problem prevented the observation of the directly diffracted light, a reflected image could be seen by the RSC. This allows the SUMER team to perform all the alignment and focussing activities foreseen, including the observations of the solar limb and sunspots (Wilhelm et al., 1997a; Lemaire et al., 1997).

## 2.4 The Spectrograph

The SUMER spectrograph consists of a selectable entrance slit, a second off-axis paraboloidal mirror (the collimator), which collimates the radiation leaving the slit, a flat mirror (the scan mirror), which deflects the beam onto the grating, a concave grating in a Wadsworth configuration (Wadsworth, 1896) and two detectors. The optical elements of the spectrograph produce a stigmatic image of the selected slit on the detector such that each spatial pixel of a spectral line corresponds to a distinct section of the solar atmosphere of approximately  $1''$  in angular size seen along the line of sight. During observations, one of the following four slit sizes can be selected:  $4'' \times 300''$ ,  $1'' \times 300''$ ,  $1'' \times 120''$ , and  $0.3'' \times 120''$ . The  $120''$  slits can each be positioned at three different detector locations. Some important spectrograph parameters are: wavelength ranges from  $465 \text{ \AA}$  to  $800 \text{ \AA}$  in second order (limited by normal-incidence reflections at short wavelengths) and from  $660 \text{ \AA}$  to  $1610 \text{ \AA}$  in first order, a collimator focal length of 399.60 mm, a grating ruling of 3600.42 lines per millimetre, and a grating radius of 3200.78 mm.

## 2.5 The Detectors

Both detectors, which are individually aligned with the focal surface of the grating, can alternatively be used to collect stigmatic images of the slit. They are of the Cross Delay-Line (XDL) type (Siegmond et al., 1995). Detector A covers the wavelength range from  $780 \text{ \AA}$  to  $1610 \text{ \AA}$  in the first order of diffraction, while detector B covers the  $660 \text{ \AA}$  to  $1500 \text{ \AA}$  range in first order. Second-order lines are superimposed on the first-order spectrum. Each detector has a Micro-Channel Plate (MCP) array of  $1024$  (spectral)  $\times$   $360$  (spatial) pixels ( $26.5 \mu\text{m} \times 26.5 \mu\text{m}$  in average size<sup>1</sup>) and observes a spectral window of  $\approx 44 \text{ \AA}$  in first order at any one time. This can be telemetered to the ground in full, but, for the sake of telemetry-rate economy, smaller spectral windows can be extracted as well. The window can be shifted across the full wavelength range of the instrument with the help of the scan mirror. The angular scale of a detector pixel at  $800 \text{ \AA}$  is  $1.03''$ , while at  $1600 \text{ \AA}$  it is  $0.95''$ . A pixel corresponds to  $45.0 \text{ m\AA}$  at  $800 \text{ \AA}$  and  $41.8 \text{ m\AA}$  at  $1600 \text{ \AA}$  in the first-order spectrum.

The photocathode surfaces of the detectors are divided into a number of sections. Two small sections of  $\approx 50$  pixels at both extremes of each photocathode are covered with grids that transmit only  $\approx 10 \%$  of the incident radiation. These attenuators are used to enable the observation of very bright emission lines, such as  $\text{H I Ly } \alpha$ , while protecting the detector from overexposure. The next  $\approx 210$  pixels on both sides of the MCP are uncoated (called “bare” MCP), whereas the central  $\approx 490$  pixels are coated with potassium bromide (KBr). The responsivity of this section is higher than that of the bare parts over most of the first-order wavelength range. Therefore, a comparison of the signal of a particular line recorded on the KBr photocathode with its response obtained from the bare part of the MCP can, in most cases, unambiguously reveal if a line is seen in first or second order.

---

<sup>1</sup>The spectral pixel size of detector A is  $26.6 \mu\text{m}$ .

## 2.6 The Electronics

The Data Processing Unit (DPU) is the central computer unit of the SUMER instrument. The DPU interfaces to the following units: the XDL detectors A and B; the motor controllers driving the various mechanisms, i.e. the front cover, the telescope pointing in east-west and in north-south directions, the slit selection, the slit focus, the grating scan, and the grating focus; the RSC; the power converter; and the spacecraft. The DPU performs the following basic tasks: switching the power of all SUMER systems; instructing the motor controllers; controlling the XDL detectors A and B; accumulating the detector data in the Image Integration Memories (IIM); controlling the RSC and collecting its images; storing image data acquired by the IIMs and the RSC; acquiring housekeeping data; transferring image and housekeeping data to the spacecraft for transmission; receiving telecommands from the spacecraft; handling of time signals; and performing fault analysis on itself and the systems connected.

The IIMs are the data collection units of the XDL detectors. They accumulate the data stream coming from the active detector. Two IIM units allow the collecting of input data signals without any time gaps: while one IIM accumulates the data, the other one can be read out. They can be erased while the data are transferred to the mass memory with a capacity of  $5 \times 10^6$  bytes.

## 2.7 Software and SUMER Command Language

The software to be executed by the DPU consists of functional packages in several layers: boot controller programme; main programmes, telemetry, telecommand, housekeeping; observational programmes written in SUMER Command Language (SCL); submodes and special functions; and hardware interfacing software.

An observer can either call up one of the available Pre-defined Operational Programmes (POP) or has to prepare a special observational sequence in SCL code. The latter sequence is called a User-Defined Programme (UDP). The SCL is a problem-oriented programming language. It was designed to satisfy the requirements of the SUMER measurement tasks. The source code of a UDP written in SCL is converted to a computer-independent metacode. This code can be loaded to the DPU and executed by an on-board interpreter. The POPs reside permanently in the DPU. One of them is the POP that generates the full-Sun images. POPs can be called up with specific parameters, such as wavelength and step width. The alphanumeric symbols used to express the elements of the SCL language are derived from the “C” and the “OCCAM” programming languages.

## 2.8 Radiometric Ground Calibration

The instrument was radiometrically calibrated against the Berlin Electron Storage ring for SYNchrotron radiation (BESSY I) as a primary source standard with the help of a transfer source standard based on a hollow-cathode discharge lamp. An assessment of the accuracy for the spectral range from 584 Å to 1236 Å (reliably calibrated in the laboratory), gave relative standard uncertainties of approximately 12 % (Hollandt et al., 1996). A thorough cleanliness programme at instrument and spacecraft levels, specifically aimed at chemical contamination control, resulted in an excellent radiometric stability of the normal-incidence optical system as well as of the detectors (Schühle, 1993; Schühle et al., 1998; Thomas, 2002).

Although it is not relevant in the context of this catalogue, it should be mentioned for completeness that the polarization sensitivity of the critical elements of the SUMER optics was measured at the SUPER Anneau de Collision d’Orsay (SUPERACO) positron storage ring to be between  $\approx 0.3$  and 0.6 (Hassler et al., 1997).

## Chapter 3

# Performance during Solar Observations

### 3.1 Spatial Resolution

The spatial resolution of SUMER is determined by the point spread function (PSF) of the telescope, the width of the active slit, the step width, the pixel size of the detectors, and the stability of the pointing of both *SOHO* and SUMER in combination with the sampling time per pointing position (Wilhelm et al., 1995b). The PSF of the telescope was measured in the laboratory to be  $0.7''$  full-width at half maximum (FWHM). The angular pixel size depends somewhat on the wavelength, but is close to  $1'' \times 1''$  (Wilhelm et al., 1995a). During the early observations from *SOHO*, the smallest solar structures found along the slit were  $2''$  (FWHM) and  $1.2''$  (FWHM) perpendicular to the slit when scanning the narrowest slit of  $0.3''$  with the smallest step width of  $0.375''$  (Lemaire et al., 1997). These data confirm the basic instrumental capabilities, as can be seen in Figure 3.1. The actual spatial resolution achieved for a specific image, however, has to be evaluated individually.

### 3.2 Spectral Resolution

The spectral resolution, although one of the most important parameters of the SUMER spectrograph, is not very critical in the context of this atlas, which is focussed on the morphology of the solar atmosphere. The spectral resolution elements determined by the grating and the detector pixel size are  $\approx 44 \text{ m}\text{\AA}$  in first order and  $\approx 22 \text{ m}\text{\AA}$  in second order of diffraction. They are adequate to resolve most of the important bright emission lines in the SUMER wavelength range, and thus allowed us to produce “pure” solar images in many spectral lines. To demonstrate this point, we have calculated average spectral profiles for the emission lines used in this work. They are displayed in Figures 3.2 to 3.5. The average spectral radiances,  $L_\lambda$ , are given in instrumental units in these diagrams. They can be converted into physical units with the help of the calibration factors provided in each of the panels. These factors have been determined with the SUMER radiometric calibration programme (cf. Section 3.4) for the central wavelengths of the lines.

Note that the widths of these profiles are broadened relative to single-pixel profiles by averaging over the slit length and all positions on the Sun. Shown by bars above the profiles are the wavelength ranges in those cases in which the spectral integration over the emission lines has been performed after transmission of the data to the ground (in Figures 3.2 and 3.5). These ranges have also been used for the calculation of the radiances and irradiances in Sections 5.6 and 5.7. In Figures 3.3 and 3.4, wavelength ranges covering 50 spectral pixels are shown in each panel for those windows that were integrated on board. The spectra displayed in these figures have been taken from the related studies carried out before or after the full-Sun images were exposed.

It should be mentioned that the limited telemetry rate available for SUMER only allowed relatively slow scan rates (and thus very long total durations for a complete image of the solar disk) with spectral information. In the interest of faster scans, the spectral integration was therefore performed on board in some cases.

For the sake of completeness, it must be mentioned that line shifts and broadenings can be measured with sub-pixel resolution. For instance, a line-of-sight velocity sensitivity of  $\approx 1 \text{ km s}^{-1}$  has been obtained (Dammasch et al., 1999b, Hassler et al., 1999), which corresponds to  $\approx 0.1$  pixel.

### 3.3 Thermal Stability

Since the beginning of March 1996, the temperature sensors of the telescope/spectrograph compartment are controlled to within  $\Delta T = \pm 0.05 \text{ K}$ , and no further drift of the optical system caused by thermal effects has been observed so far. But even these small quasi-periodic temperature variations lead to alignment offsets, which have to be taken into account in some critical cases (cf. Dammasch et al., 1999b; Rybak et al., 1999).

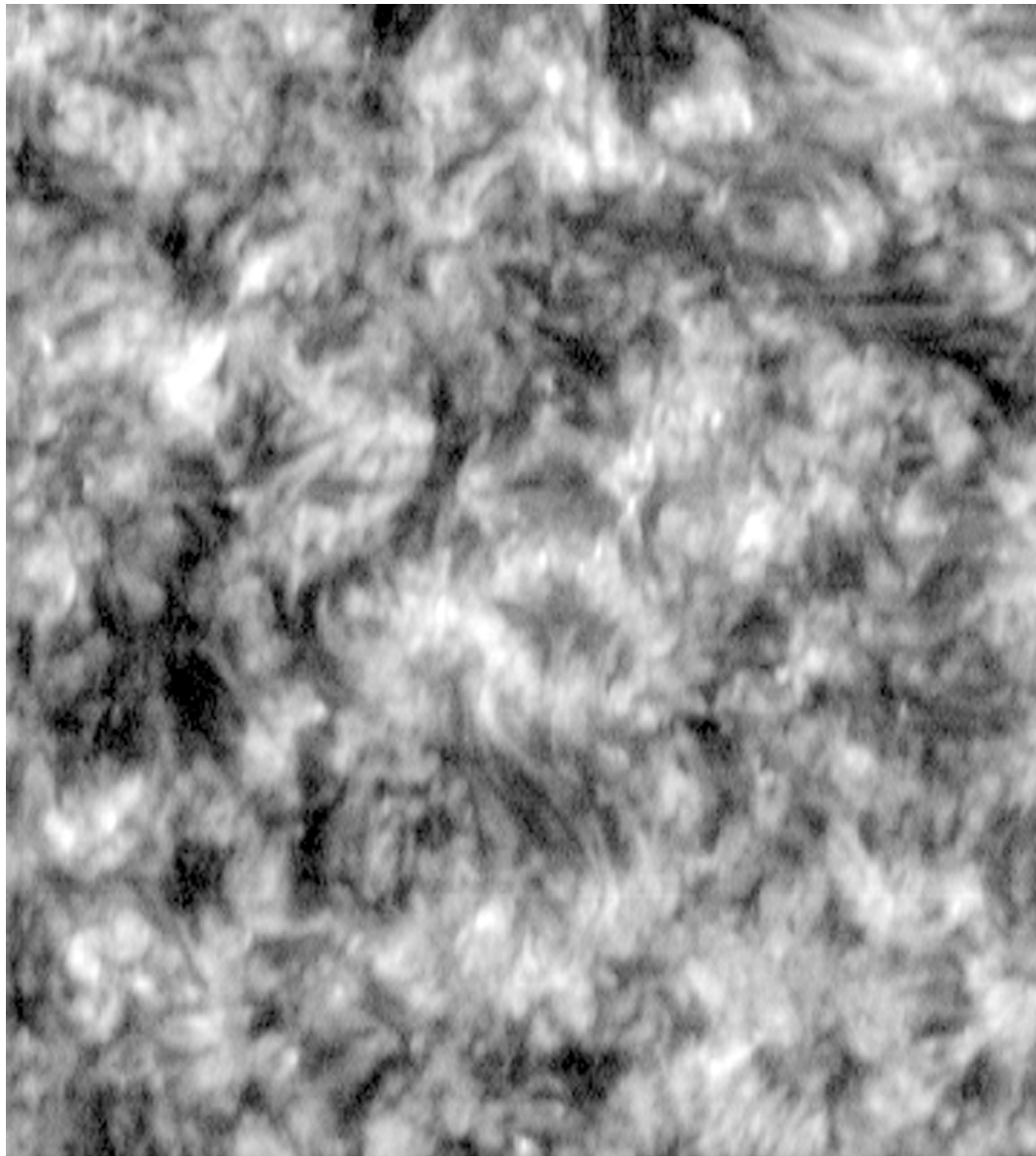


Figure 3.1: Observations of the quiet Sun in the O VI 1032 Å line on 30 January 1996. The area displayed has an angular extension of  $273'' \times 300''$  and a size of  $193 \text{ Mm} \times 212 \text{ Mm}$ . It is situated near the centre of the solar disk.

### 3.4 Inflight Radiometric Calibration

In order to establish a radiometric characterization in spectral ranges at wavelengths shorter and longer than could be covered on the ground, we compared line-radiance ratios measured on the solar disk with the results of atomic physics calculations. We also evaluated SUMER stellar observations and obtained radiometric information with the help of the *International Ultraviolet Explorer (IUE)* and *Hubble Space Telescope (HST)* standard stars (Wilhelm et al., 1997b; Hollandt et al., 1998; Schühle et al., 2000). The *IUE* data agreed with SUMER observations near 1200 Å, where both instruments overlap in their wavelength ranges. Comparisons with the Coronal Diagnostic Spectrometer (CDS) on *SOHO* (Harrison et al., 1995) and with the SOLAR-STellar Irradiance Comparison Experiment (SOLSTICE) on the *Upper Atmosphere Research Satellite (UARS)* (Rottman et al., 1993) have also been performed successfully (Pauluhn et al., 2001a, b, 2002; Wilhelm et al., 1999a).

In a comparison between a coronal spectrum obtained by SUMER and the CHIANTI database, Landi et al. (2002) found that the observed ratio of the Si XII lines at 499 Å and 520 Å agrees very well with the theoretical predictions. Moreover, there is no evidence for any other gross inaccuracy in the full SUMER wavelength range.

When applying the spectral responsivity functions to solar measurements, it is necessary to take into account the exact slit dimensions and the vignetting effects of field stops as well as the diffraction at the slits. This can be accomplished by applying the SUMER calibration programme `radiometry.pro`. This programme can be found in the software tree of Solarsoft at <http://soho.nascom.nasa.gov/solarsoft/soho/sumer/idl/contrib/wilhelm/rad/>.

It is under configuration control (Wilhelm et al., 2002). The relative uncertainties in the central wavelength range are 15 % for detector A and 20 % for detector B before the attitude loss of *SOHO* in 1998. After the recovery larger uncertainties of 33 % and 36 %, respectively, have to be expected.

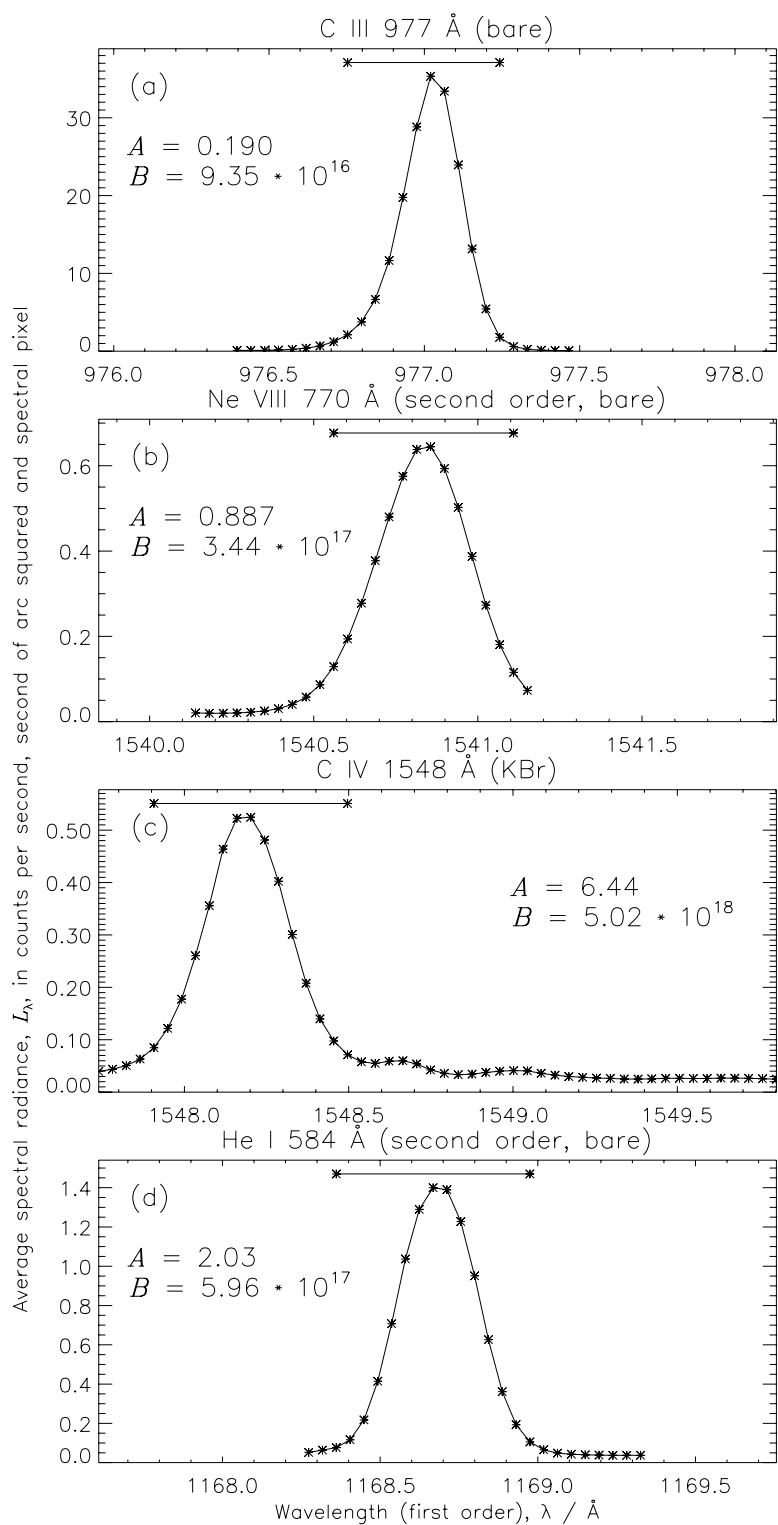


Figure 3.2: Profiles of spectral lines for which full-Sun images are available with complete spectral information. The bars above the profiles show the wavelength ranges over which the spectral integrations were performed. (a) C III 977  $\text{\AA}$  line. Calibration factors are:  $A$  to get the spectral radiance,  $L_\lambda$ , in units of  $1 \text{ W m}^{-2} \text{sr}^{-1} \text{\AA}^{-1}$ , and  $B$  to get  $L_\lambda$  in photons per second, square metre, steradian and  $\text{\AA}$ , (b) Ne VIII 770  $\text{\AA}$  (in second order), (c) C IV 1548  $\text{\AA}$ , and (d) He I 584  $\text{\AA}$  (in second order).

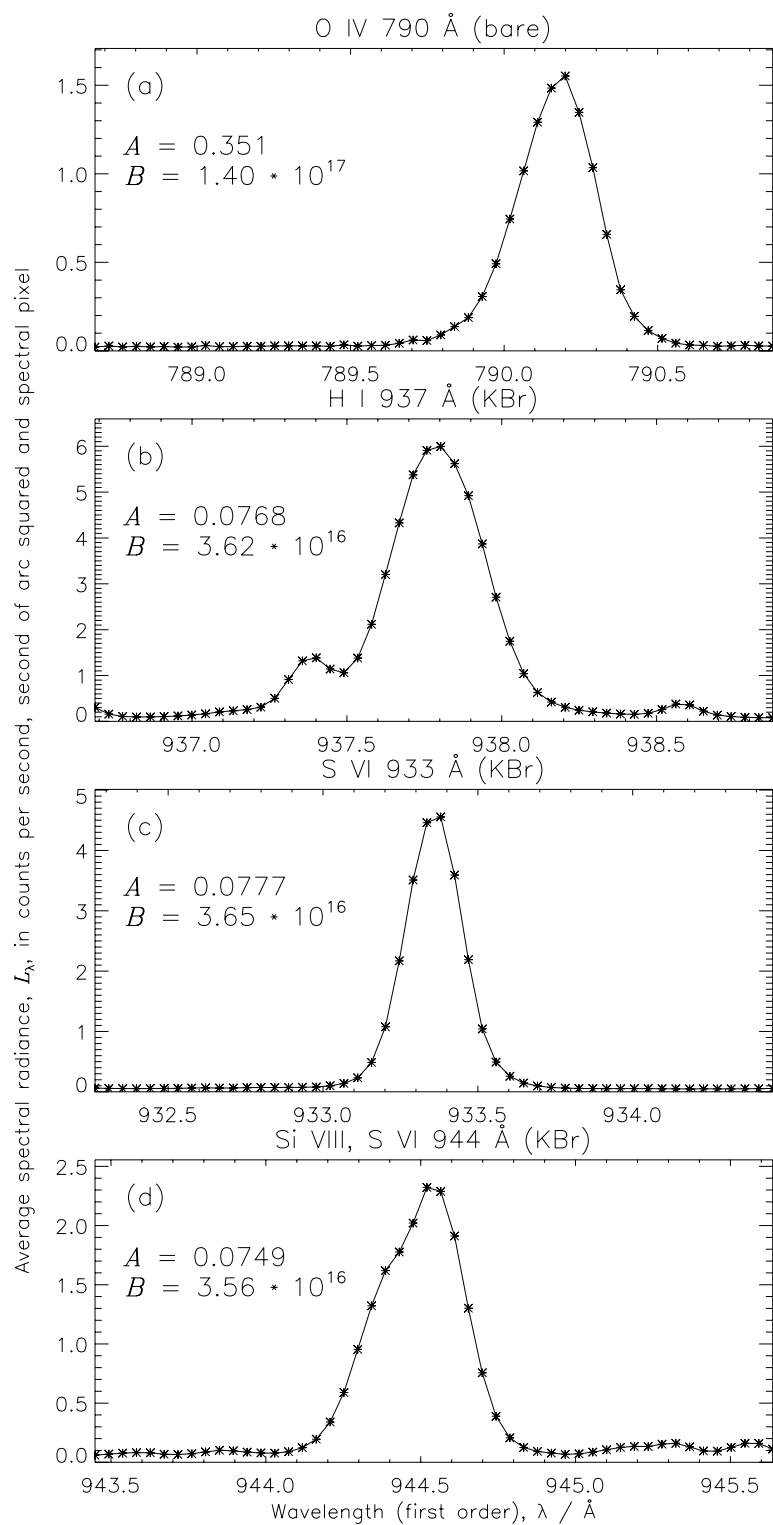


Figure 3.3: Profiles of (a) O IV 790  $\text{\AA}$ , (b) H I 937  $\text{\AA}$  (note the He II Balmer 10 line at 937.4  $\text{\AA}$ ), (c) S VI 933  $\text{\AA}$ , and (d) S VI 944  $\text{\AA}$  (blended with the Si VIII 944  $\text{\AA}$  line, which causes the relatively strong coronal radiation in the image on page A.56). Calibration factors as in Figure 3.2.

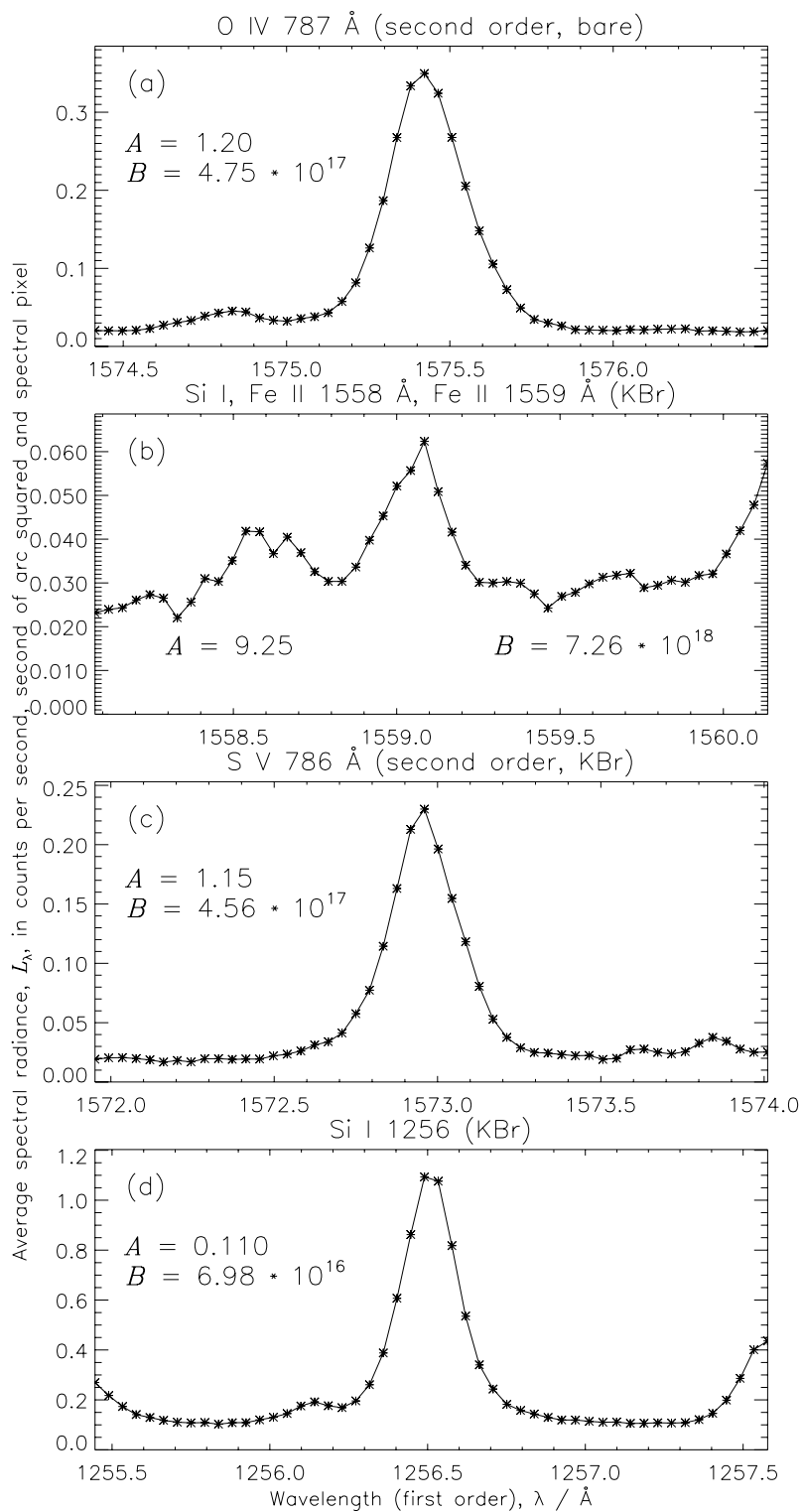


Figure 3.4: Profiles of (a) O IV 787 Å (in second order), (b) Fe II 1559 Å, (c) S V 786 Å (in second order), and (d) Si I 1256 Å.

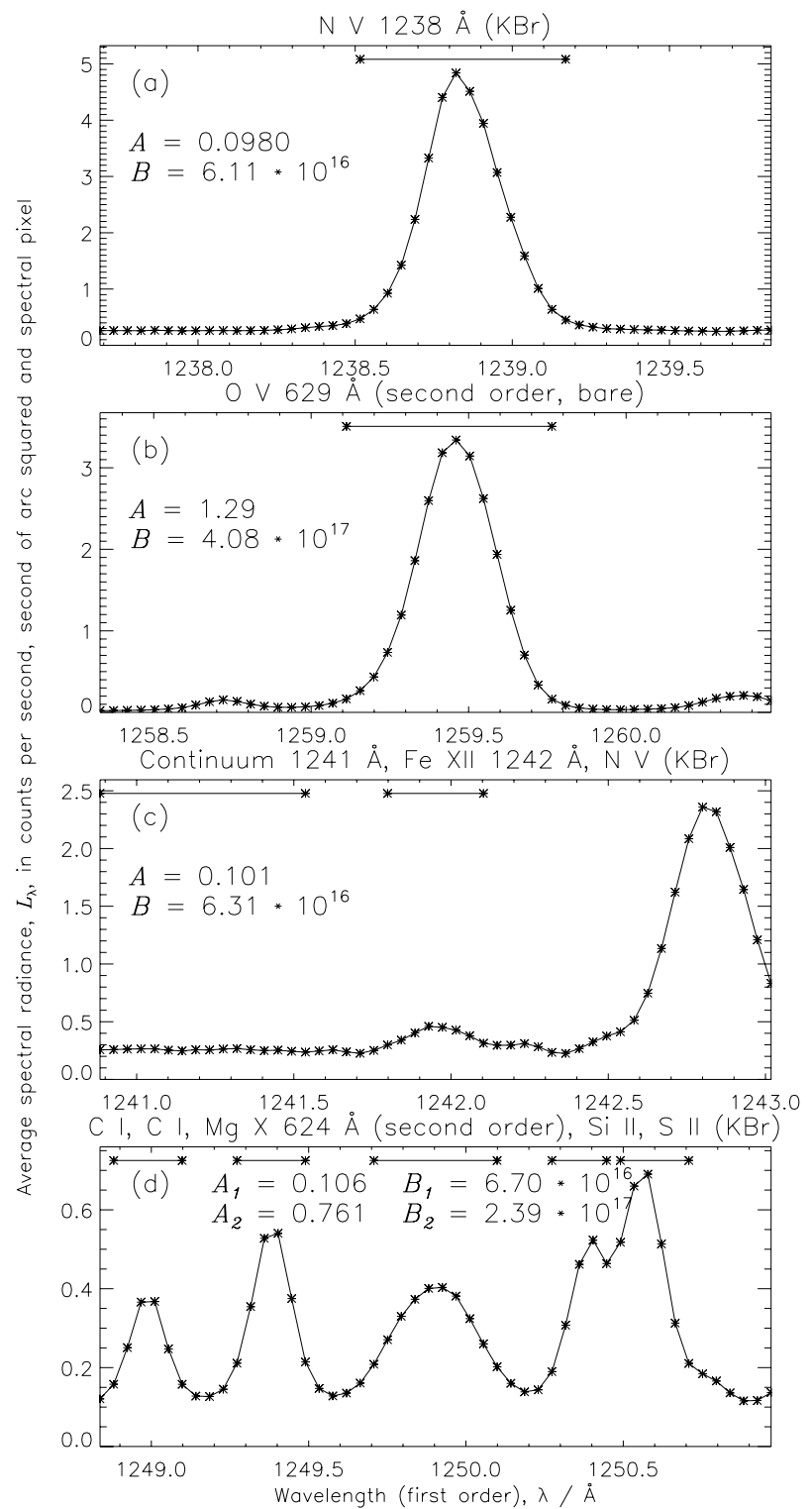


Figure 3.5: Spectra transmitted during the Full-Sun Month period (cf. Section 5.5) with profiles of (a) N V 1238 Å, (b) O V 629 Å (in second order), (c) Fe XII 1242 Å, and (d) Mg X 624 Å (in second order), with C I, Si II and S II in first order. Calibration factors are given for both orders.

## Chapter 4

# Image Processing

All images presented on pages A.2 to A.209 of the atlas were rastered with SUMER slit No 2 ( $1'' \times 300''$ ). Spectrally resolved images have been transmitted for four full-disk scans in C III, Ne VIII, C IV, and He I (see Figure 3.2 and Section 5.2), and for the images of the Whole-Sun Month (cf. Section 5.5). In the case of the S VI time series (Section 5.4), the continuum level was subtracted before spectral integration on board.

In the atlas section showing selected images in full resolution, information about the spectral line, its wavelength, the step width and the integration time are given at the top of the page, whereas the raster start time and the end, as well as the corresponding solar east-west coordinates,  $x_0$  and  $x_1$ , are given under each image together with the north-south coordinate,  $y$ , of the slit centre. The detailed images are cut into halves to fit on the pages. The full-disk images are arranged such that the centre of the solar disk is in the centre of the image, and the image extends from  $1011''$  east to  $1011''$  west in solar coordinates. The spectral line, its wavelength, the raster step, and integration time are given at the top of each page. At the bottom the start and end times are given. A few images were taken before the *SOHO* and instrument commissioning phases had been completed, and were not correctly centred. Missing parts of the disk due to this fact or due to data faults during the transmission to ground have been restored in grey shade up to the chromospheric limb.

The relatively small spectral windows of 25 pixels around C III 977 Å and Ne VIII 770 Å are dominated by these lines, and no background level could be established. On the other hand, the line He I 584 Å could be separated from the surrounding continuum to produce a continuum image despite the small spectral window. A separate continuum image could also be produced without difficulty from the wide spectral window of 50 pixels around the C IV 1548 Å line. The two images taken around 804 Å and 812 Å in the H I Lyman continuum were added to get a better signal-to-noise ratio. Since their morphology was identical, no information was lost.

For a series of fifteen images (five scans with three lines each) in June 1996, three spatial pixels in the north-south direction were binned on board (Section 5.3). The spectral window around the Fe II 1559 Å line is blended with Si I and a relatively strong continuum, and thus large corrections had to be applied. The O V 629 Å line was originally blended with Si I and Si II, but this effect was removed by subtracting an image obtained in Si I multiplied with an appropriate factor. The scan of 15 June 1996 was interrupted 15 min before its completion, because a Joint Observational Programme (JOP) had been scheduled at that time. On 26 June 1996, the scan in He I 584 Å was performed three times, but the first two scans were interrupted in the middle, because this observation was performed in support of a sounding rocket calibration programme (cf. Wilhelm, 2002) and had to be synchronized with the rocket launch schedule.

Full-disk images were scanned in eight overlapping horizontal scans (“swaths”). Most of them were obtained with the full-Sun POP (cf. Section 2.7), and were started in the south-east corner with an east-west scan, followed by a west-east scan  $270''$  further north, and so on. Only the He I full disks of 2 March and 26 June 1996 were produced with a UDP, and were started in the north-east corner with an east-west scan, followed by a west-east scan  $290''$  further south, and so on.

To assemble the full-disk images from the eight swaths, the overlap was determined by means of a correlation calculation. The overlap was then generally split into halves, taking one part from the northern and one part from the southern image. To make the full-disk images look smoother at the borders of the swaths, the effect of solar rotation was compensated on both sides of the borders as far as possible. One has to keep in mind though that these assembled full-disk images never represent a snapshot of the whole Sun at a certain moment.

Between March and October 1996, 37 studies were run in which the full disk was rastered in the H I and S VI lines with full spatial resolution (see Section 5.4). Usually, the lines H I 937 Å, S VI 933 Å and S VI 944 Å were observed. However, in the last few studies following 6 September 1996, S VI 944 Å was replaced by H I Ly $\delta$ , but this line is not considered here. One study of the S VI time series (that of 12 May 1996) was selected to be shown with full resolution in Section 5.2, the study of 21 June 1996 had many data errors, and another one of 28 August 1996 was interrupted in the middle. The full-disk images of the remaining 34 studies are displayed in two of the three spectral lines each, usually in H I 937 Å and S VI 933 Å.

Between 10 August 1996 and 9 September 1996, the Whole-Sun Month study was executed 34 times by SUMER in various solar locations (northeast, northwest, southeast, southwest, polar coronal hole boundary, off limb, streamer, equatorial coronal hole; see Section 5.5). Each observation consists of an  $\approx 720'' \times 300''$  scan with a raster step of width  $1.5''$  and an exposure time of 60 s, simultaneously taken and transmitted in four different windows of 50 spectral pixels

each (cf. Figure 3.5). The following data were selected: from the interval around 1239 Å the N v 1238 Å line, from the interval around 1259 Å the second order O v line, from the interval around 1242 Å the Fe xii line and the 1241 Å continuum, and from the interval around 1245 Å, two C i lines, the second order Mg x line, the Si ii line, and the S ii line. The first interval contains some pixels with continuum radiation, but they are often influenced by the very strong and dynamic N v line at 1238 Å. The second interval also contains some continuum radiation and a Si i line, but both are often affected by the strong and dynamic O v line. The third interval contains parts of the N v line at 1242 Å, but this line is not used. The Fe xii line is weak and blended with several chromospheric lines. It can, however, be resolved by subtracting the continuum multiplied with an appropriate factor. The continuum at 1241 Å appears to be the purest of all four intervals. The fourth interval contains two C i lines which were added for the images; the Si ii and S ii lines are blended, but could be resolved by Gaussian fitting.

Thus, eight different images – showing the Sun from the lower chromosphere at a temperature of  $1 \times 10^4$  K to the corona at  $1.4 \times 10^6$  K – could be created from each scan. On the top of each page, the start and end times of the scan are given, as well as the solar coordinates; the relevant spectral information is stated next to each image.

For images transmitted in full spectral resolution, it had to be determined which part of the 25 or 50 pixels should be used for the integration over the spectral range. As mentioned before, the selected intervals are marked with horizontal lines in the spectral windows of Figures 3.2 and 3.5. The level of the continuum was then estimated and subtracted. The deadtime and local-gain corrections were performed with the standard SUMER software. In the case of full disks that were spectrally integrated on board a gain correction could not be performed; however, for the irradiance calculations in Tables 5.8 and 5.9, the gain correction was estimated. The flat-field corrections were performed with a method described in Dammasch et al. (1999b). Minor data faults were eliminated by substituting the average values of neighbouring slit images.

## Chapter 5

# Description of Images

### 5.1 General Considerations

As outlined in Chapter 4, the images displayed in the atlas on pages A.2 to A.209 are organized into four groups. The first group consists of eleven full-Sun images recorded with spatial resolution elements of  $1.13'' \times 1.0''$ ,  $1.5'' \times 1.0''$  or  $1.88'' \times 1.0''$ , and integration times that varied between 3 s and 15 s. Since it is not possible to resolve the fine morphological details that SUMER achieved with the naked eye when the high-resolution full-Sun images are plotted at a diameter of 28 cm on a single atlas page, we also include the entire set of partial images from which the full-Sun images were assembled. The second group includes 16 full-Sun images of which several were recorded simultaneously with spatial resolution elements of  $3'' \times 3''$ . The third group includes a time sequence of 34 sets of simultaneously recorded H I Ly $\epsilon$  images, and those of S VI at 933 Å and 944 Å, generally with resolution elements of  $1.5'' \times 1.0''$ . The last group includes 34 sets of partial-Sun images of mostly coronal-hole boundaries in various solar locations. All images have brief figure captions providing the basic information for their identification. The start of an east-west scan is at  $x_o$ , and  $x_1$  is the stop coordinate. In the interest of an unambiguous identification of the images, an internal reference code is added in parentheses, which is of no further importance in the context of this atlas.

In studying the morphological properties of the SUMER images the following should be taken into consideration:

- Average sizes of quiet-region and coronal-hole structures spanning the  $3 \times 10^4$  K to  $5 \times 10^5$  K temperature range are approximately  $1''$  wide and  $10''$  to  $20''$  long. The lifetimes of these structures in general do not exceed 10 min (Feldman, Dammasch & Wilhelm, 2000). Together with the long acquisition times of full-Sun images mentioned in Section 1.3, this leads to discontinuities along the interfaces between different swaths, which can clearly be seen. In active regions, the lifetimes of structures in the same temperature range are significantly longer. Thus when studying the SUMER quiet-region or coronal-hole images one would most likely find that shapes of structures oriented along the north-south direction are sharper than those oriented in the east-west direction. This would be the case in images where the raster speed, i.e. the step size divided by the integration time, was smaller than, say  $\delta x/\delta t = 0.03''/s$ .
- In quiet regions and coronal holes close to the centre of the Sun only small differences appear to exist between images recorded in lines representative of the  $3 \times 10^4$  K to  $5 \times 10^5$  K temperature range. However, when observing near the solar limb profound differences are present. This is also apparent when comparing the brightness of an image as a function of Sun centre distances. In some images the limb brightening is much larger than in others. Undoubtedly, the optical depth of the plasma for the line in which a particular image is formed is the main reason for this behaviour. Calculated opacities and relevant parameters for many of the lines listed in Table 1.1 are given in Table 5.1. The method used in calculating the opacities and the assumptions made regarding the plasma properties are as follows:

The opacity,  $\tau$ , of the plasma in a spectral line can be determined from

$$\tau = \frac{\sqrt{\pi} e^2 f_{ij} \lambda^2}{m_e c_0^2 \Delta\lambda_D} n_g s \quad (5.1)$$

where  $e$  is the electron charge,  $f_{ij}$  is the oscillator strength,  $m_e$  the electron mass,  $c_0$  the vacuum speed of light,  $\lambda$  the transition wavelength,  $\Delta\lambda_D$  the Doppler width,  $n_g$  the ground-level population density, and  $s$  the length of the plasma column along the line of sight (Rybicki & Lightman, 1979).  $n_g$  can be expressed as

$$n_g = \frac{n_g}{n_i} \frac{n_i}{n_X} \frac{n_X}{n_H} \frac{n_H}{n_e} n_e \quad (5.2)$$

where  $n_i$ ,  $n_X$ ,  $n_H$  and  $n_e$  are the ion, the element and the proton and electron number densities. Under typical conditions in the solar upper atmosphere the values  $n_i/n_X = F(T_e)$  can be calculated and are taken here from Arnaud & Rothenflug (1985). The elemental abundances  $n_X/n_H = A_{Ab}$  are taken from Grevesse & Sauval (1998),

Table 5.1: Calculated opacities and relevant plasma parameters.

Spectral line	He I	O V	O IV	S VI	C III	O VI	N V	C IV
Wavelength, $\lambda/\text{\AA}$	584	629	790	933	977	1032	1238	1548
Oscillator strength <sup>a</sup> , $f_{ij}$	0.28	0.53	0.15	0.425	0.81	0.131	0.156	0.19
Electron temperature, $T_e/(10^5 \text{ K})$	0.3	2.5	1.6	2.0	0.7	3.0	1.8	1.1
Electron density, $n_e/(10^9 \text{ cm}^{-3})$	33	4.0	6.3	5.0	14.3	3.3	5.6	9.1
Elemental abundance, $A_{\text{Ab}}/10^{-4}$	600	6.76	6.76	0.214	3.31	6.76	0.832	3.31
Ionic fraction <sup>b</sup> , $F(T_e)$	0.9	0.46	0.68	0.12	0.81	0.23	0.25	0.35
Level population, $n_g/n_i$	1.0	1.0	0.67	1.0	1.0	1.0	1.0	1.0
Doppler width, $\Delta\lambda_D/\text{\AA}$	0.14	0.08	0.10	0.12	0.13	0.13	0.16	0.2
Opacity for $10^3 \text{ km}$	450	1.26	0.71	0.015	0.24	0.210	0.07	0.94

<sup>a</sup> Data are taken from Bar-Shalom, Klapisch & Oreg (2001).

<sup>b</sup> Arnaud & Rothenflug (1985).

and a good approximation for  $n_{\text{H}}/n_e$  is 0.8. The  $n_g/n_i$  values are derived using the Hebrew University Lawrence Livermore Atomic Code (HULLAC) (Bar-Shalom, Klapisch & Oreg, 2001). In most cases, these values are close to unity, but can deviate from this value for metastable levels.

Throughout the calculations we assumed that the plasmas in the  $3 \times 10^4 \text{ K}$  to  $5 \times 10^5 \text{ K}$  temperature range are at a constant pressure of  $n_e T_e = 1 \times 10^{15} \text{ K cm}^{-3}$  (cf. Mariska, 1992); we also assumed a constant  $\Delta\lambda/\lambda$  based on a value,  $\Delta\lambda_D$ , of  $0.2 \text{ \AA}$  for the C IV 1548  $\text{\AA}$  line. For He I, however, we used a measured value. Because all the lines in Table 5.1 are emitted by elements with high first-ionization potentials (FIP), their abundances in the solar upper atmosphere are the same as in the photosphere.

- Boundaries between coronal-hole and quiet-Sun regions are easily observed in H I or He I images. The same cannot be said about images that are observed in transition-region lines with typical formation temperatures of  $2 \times 10^4 \text{ K} < T_F < 6 \times 10^5 \text{ K}$  emitted by elements other than hydrogen and helium. Thus, when viewing the SUMER images, attention should be paid to the excitation properties of the lines in which the images were formed, and, in particular, to the ratio between the excitation energy of the line and the formation temperature of the ion. Collisional cross-sections of spectral lines have a temperature dependence of the form  $T_e^{-1/2} \exp[-\Delta E/(k T_e)]$ , where  $\Delta E$  is the excitation energy of the line, and  $k$  is the Boltzmann constant.

Whereas the He I line originates in plasmas having electron temperatures that typically do not exceed  $3 \times 10^4 \text{ K}$ , corresponding to  $k T_e = 2.7 \text{ eV}$ , the excitation energy of the 584  $\text{\AA}$  line is significantly higher at  $\Delta E = 21 \text{ eV}$  resulting in a factor of  $\Delta E/k T_e = 7.8$ . For the images produced by lines other than the chromospheric ones, the excitation energies and formation temperatures are fairly close to each other. As examples may serve the O IV 787  $\text{\AA}$  line that is typically emitted from a temperature of  $T_e \approx 1.7 \times 10^5 \text{ K}$  (15 eV) and has an excitation energy of 16 eV, resulting in  $\Delta E/k T_e = 1.1$ , and the O V 629  $\text{\AA}$  line that is typically emitted from a plasma of  $T_e \approx 2.5 \times 10^5 \text{ K}$  ( $\approx 22 \text{ eV}$ ) and has an excitation energy of 20 eV, resulting in  $\Delta E/k T_e = 0.91$ . For the He I and H I images relatively small changes in temperature will thus cause large variations in brightness, whereas the brightness in the other images will be significantly less sensitive to temperature variations.

## 5.2 Full-Sun Images at Highest Spatial Resolution

This section of the atlas consists of a collection of eleven full-Sun images with step sizes of  $1.13''$ ,  $1.50''$ , and  $1.88''$ , i.e. with multiple steps of three, four, or five basic widths (cf. Section 1.3), recorded between 28 January 1996 and 13 May 1996 (for a list of images, their acquisition dates, exposure times and step sizes see Table 5.2). The collection includes two individually recorded images in the C III 977  $\text{\AA}$  and Ne VIII 770  $\text{\AA}$  lines, three simultaneously recorded pairs of images in the C IV 1548  $\text{\AA}$  line and the 1549  $\text{\AA}$  continuum, in the O IV 790  $\text{\AA}$  line and the 812  $\text{\AA}$  continuum, and in the He I 584  $\text{\AA}$  line and the 1169  $\text{\AA}$  continuum. In addition, it includes three simultaneously recorded images in the H I 937  $\text{\AA}$  (Ly $\epsilon$ ) line, and in the S VI lines at 933  $\text{\AA}$  and 944  $\text{\AA}$ . The C III image was exposed in normal-step mode, the other images in smear-step mode.

It should be noted that the free-bound H I Ly continuum is the main contributor in the 812  $\text{\AA}$  continuum band. It should also be mentioned that the 944  $\text{\AA}$  window contains a blend of the S VI resonance line with a forbidden Si VIII line (cf. Section 3.2 and Figure 3.3d for line profile information).

Table 5.2: Full-Sun and partial images with  $1.13'' \times 1.0''$ ,  $1.5'' \times 1.0''$ , or  $1.88'' \times 1.0''$  resolution elements.

Atlas page	Start date 1996	Line, continuum Wavelength, $\lambda/\text{\AA}$	Area	Step size, $\delta x/''$	Exposure time, $\delta t/s$
A.2	29 January	C III 977	northeast	1.13	7.25
A.3	29 January	C III 977	northwest	1.13	7.25
A.4	28 January	C III 977	southeast	1.13	7.25
A.5	28 January	C III 977	southwest	1.13	7.25
A.6	28 January	C III 977	full disk	1.13	7.25
A.7	2 February	Ne VIII 770	full disk	1.88	7.5
A.8	2 February	Ne VIII 770	northeast	1.88	7.5
A.9	2 February	Ne VIII 770	northwest	1.88	7.5
A.10	2 February	Ne VIII 770	southeast	1.88	7.5
A.11	2 February	Ne VIII 770	southwest	1.88	7.5
A.12	4 February	C IV 1548	northeast	1.88	15.0
A.13	4 February	Cont 1549	northeast	1.88	15.0
A.14	4 February	C IV 1548	northwest	1.88	15.0
A.15	4 February	Cont 1549	northwest	1.88	15.0
A.16	4 February	C IV 1548	southeast	1.88	15.0
A.17	4 February	Cont 1549	southeast	1.88	15.0
A.18	4 February	C IV 1548	southwest	1.88	15.0
A.19	4 February	Cont 1549	southwest	1.88	15.0
A.20	4 February	C IV 1548	full disk	1.88	15.0
A.21	4 February	Cont 1549	full disk	1.88	15.0
A.22	27 February	O IV 790	northeast	1.50	6.0
A.23	27 February	Cont 804, 812	northeast	1.50	6.0
A.24	27 February	O IV 790	northwest	1.50	6.0
A.25	27 February	Cont 804, 812	northwest	1.50	6.0
A.26	27 February	O IV 790	southeast	1.50	6.0
A.27	27 February	Cont 804, 812	southeast	1.50	6.0
A.28	27 February	O IV 790	southwest	1.50	6.0
A.29	27 February	Cont 804, 812	southwest	1.50	6.0
A.30	26 February	O IV 790	full disk	1.50	6.0
A.31	26 February	Cont 804, 812	full disk	1.50	6.0
A.32	2 March	He I 584	northeast	1.50	7.0
A.33	2 March	Cont 1169	northeast	1.50	7.0
A.34	3 March	He I 584	northwest	1.50	7.0
A.35	3 March	Cont 1169	northwest	1.50	7.0
A.36	3 March	He I 584	southeast	1.50	7.0
A.37	3 March	Cont 1169	southeast	1.50	7.0
A.38	3 March	He I 584	southwest	1.50	7.0
A.39	3 March	Cont 1169	southwest	1.50	7.0
A.40	2 March	He I 584	full disk	1.50	7.0
A.41	2 March	Cont 1169	full disk	1.50	7.0
A.42	13 May	H I 937	northeast	1.50	3.0
A.43	13 May	S VI 933	northeast	1.50	3.0
A.44	13 May	H I 937	northwest	1.50	3.0
A.45	13 May	S VI 933	northwest	1.50	3.0
A.46	12 May	H I 937	southeast	1.50	3.0
A.47	12 May	S VI 933	southeast	1.50	3.0
A.48	12 May	H I 937	southwest	1.50	3.0
A.49	12 May	S VI 933	southwest	1.50	3.0
A.50	12 May	H I 937	full disk	1.50	3.0
A.51	12 May	S VI 933	full disk	1.50	3.0
A.52	13 May	S VI 944	northeast	1.50	3.0
A.53	13 May	S VI 944	northwest	1.50	3.0
A.54	12 May	S VI 944	southeast	1.50	3.0
A.55	12 May	S VI 944	southwest	1.50	3.0
A.56	12 May	S VI 944	full disk	1.50	3.0

### 5.3 Full-Sun Images with Reduced Resolution

This section of the atlas consists of six separate sets of images, of which the first five contain three simultaneously recorded images each, and the last of a single image (see Table 5.3). One image in both the first and the fifth sets was recorded in the Li-like C IV 1548 Å line, a second in the B-like O IV 787 Å line, and the third in the Li-like Ne VIII 770 Å line. The second and the third sets were recorded in the Li-like N V 1238 Å line, the Be-like O V 629 Å line, and in the Si I 1256 Å line. The fourth set was recorded again in the O IV 787 Å line, in the Mg-like S V 786 Å line, and in the Fe II 1559 Å line. The last image in the group is the He I 584 Å line. The contribution temperatures of these lines are listed in Table 1.1. The spatial resolution element is  $3.0'' \times 1.0''$  for He I and  $3.0'' \times 3.0''$  for the other lines. In the latter cases, three detector pixels were binned together on board. All images were exposed in smear-step mode.

The images provide morphological information on plasma structures in roughly three different domains: from  $1 \times 10^4$  K to  $3 \times 10^4$  K,  $1 \times 10^5$  K to  $3 \times 10^5$  K, and  $5 \times 10^5$  K to  $8 \times 10^5$  K. Thus a comparison between the simultaneously exposed Si I and the N V or O V images as well as between the Fe II and the O IV or S V images yields insight into the relationship between the morphologies of the chromosphere and the transition-region plasma structures. On the other hand, comparisons between simultaneously exposed Ne VIII and C IV or O IV images can clarify the relationship between the morphologies of the upper transition-region plasma structures at  $5 \times 10^5$  K to  $8 \times 10^5$  K and those of the middle transition region at temperatures of  $1 \times 10^5$  K to  $3 \times 10^5$  K.

Although the plasmas responsible for most of the emission in the C IV, N V, O IV, O V and S V lines have approximately the same temperatures, the opacities along the line of sight are vastly different (see Table 5.1), and therefore comparisons between simultaneously recorded images can provide valuable information on the physical properties of the plasmas and, in particular, on the line-of-sight dimensions of the unresolved fine structures responsible for most of the emission.

The excitation energy of the He I line is significantly larger than the temperature of the plasma from which the helium line is emitted, as was mentioned before. This is not the case for the C IV, N V, O IV and O V lines, in which the other images in this section were recorded. Thus a comparison between the properties of the images could shed light on the magnitude of any temperature fluctuations expected in various solar regions and, in particular in quiet-Sun and coronal-hole regions.

Comparisons between the simultaneously exposed Ne VIII and C IV or between the O IV images in the vicinity of regions of activity show the extent of morphological changes that result from the emergence of magnetic flux. This phenomenon is most apparent in the images of 7 June that contain small regions of activity close to the centre of the disk. Inspection of these images reveals that while the structures brighten on closed field lines of active regions, the structures diminish in brightness in surrounding regions and primarily those along network boundaries.

Table 5.3: Full-Sun images with reduced resolution elements.

Atlas page	Start date 1996	Line, Wave-length, $\lambda/\text{\AA}$	Step size, $\delta x/''$	Binning, pixel	Exposure time, $\delta t/s$
A.57	7 June <sup>a</sup>	C IV 1548	3.0	3	2.0
A.58	7 June <sup>a</sup>	O IV 787	3.0	3	2.0
A.59	7 June <sup>a</sup>	Ne VIII 770	3.0	3	2.0
A.60	7 June <sup>b</sup>	N V 1238	3.0	3	2.0
A.61	7 June <sup>b</sup>	O V 629	3.0	3	2.0
A.62	7 June <sup>b</sup>	Si I 1256	3.0	3	2.0
A.63	14 June	Si I 1256	3.0	3	2.0
A.64	14 June	N V 1238	3.0	3	2.0
A.65	14 June	O V 629	3.0	3	2.0
A.66	15 June	Fe II 1559	3.0	3	2.0
A.67	15 June	S V 786	3.0	3	2.0
A.68	15 June	O IV 787	3.0	3	2.0
A.69	16 June	O IV 787	3.0	3	2.0
A.70	16 June	C IV 1548	3.0	3	2.0
A.71	16 June	Ne VIII 770	3.0	3	2.0
A.72	26 June	He I 584	3.0	1	2.0

<sup>a</sup>Observations were performed between 15:49 and 19:33 UTC.

<sup>b</sup>Observation time: 7 June 23:40 UTC to 8 June 03:24 UTC.

## 5.4 Synoptic Studies of the Sun in H I and S VI

This section of the atlas is intended to give a synoptic portrayal of the Sun in the H I 937 Å and S VI 933 Å lines. The sequence began on 26 March 1996 and lasted until 5 October 1996, during which time 35 sets of H I and S VI images were acquired (Table 5.4; page A.73 is intentionally left blank). The Sun completed about seven rotations around its axis during the 6.2 months (194 d) of observation; thus, on average, five sets of images were obtained during each solar rotation.

The images provide a description of the long-term development of solar upper-atmosphere structures in both the chromosphere and in the middle transition region, with an order of magnitude difference in the characteristic formation temperatures of the emitted spectral lines. Although these observations were made at high resolution, the full-Sun images are shown here at reduced resolution, with the exception of the data of 12 and 13 May 1996 that have been presented in Section 5.2.

Table 5.4: A series of 34 full-Sun images in S VI and H I Ly $\epsilon$  with  $1.13'' \times 1.0''$  or  $1.5'' \times 1.0''$  spatial resolution elements obtained in smear-step mode.

Atlas page	Start date 1996	Line, Wavelength, $\lambda/\text{\AA}$	Step size, $\delta x/''$	Exposure time, $\delta t/s$
A.74	26 March	H I 937	1.50	2.0
A.75	26 March	S VI 944	1.50	2.0
A.76	1 April	H I 937	1.13	1.0
A.77	1 April	S VI 933	1.13	1.0
A.78	7 April	H I 937	1.50	3.0
A.79	7 April	S VI 933	1.50	3.0
A.80	14 April	H I 937	1.50	3.0
A.81	14 April	S VI 933	1.50	3.0
A.82	18 April	H I 937	1.50	3.0
A.83	18 April	S VI 933	1.50	3.0
A.84	24 April	H I 937	1.50	3.0
A.85	24 April	S VI 933	1.50	3.0
A.86	29 April	H I 937	1.50	3.0
A.87	29 April	S VI 933	1.50	3.0
A.88	4 May	H I 937	1.50	3.0
A.89	4 May	S VI 933	1.50	3.0
A.90	8 May	H I 937	1.50	3.0
A.91	8 May	S VI 933	1.50	3.0
A.92	17 May	H I 937	1.50	3.0
A.93	17 May	S VI 933	1.50	3.0
A.94	24 May	H I 937	1.50	3.0
A.95	24 May	S VI 933	1.50	3.0
A.96	28 May	H I 937	1.50	3.0
A.97	28 May	S VI 933	1.50	3.0
A.98	3 June	H I 937	1.50	3.0
A.99	3 June	S VI 933	1.50	3.0
A.100	8 June	H I 937	1.50	3.0
A.101	8 June	S VI 933	1.50	3.0
A.102	12 June	H I 937	1.50	3.0
A.103	12 June	S VI 933	1.50	3.0
A.104	16 June	H I 937	1.50	3.0
A.105	16 June	S VI 933	1.50	3.0
A.106	1 July	H I 937	1.50	3.0
A.107	1 July	S VI 944	1.50	3.0
A.108	6 July	H I 937	1.50	3.0
A.109	6 July	S VI 933	1.50	3.0
A.110	11 July	H I 937	1.50	3.0
A.111	11 July	S VI 933	1.50	3.0
A.112	16 July	H I 937	1.50	3.0
A.113	16 July	S VI 933	1.50	3.0

Table 5.4: Continuation of table from previous page

Atlas page	Start date <sup>a</sup> 1996	Line, Wave-length, $\lambda/\text{\AA}$	Step size, $\delta x/''$	Exposure time, $\delta t/s$
A.114	21 July	H I 937	1.50	3.0
A.115	21 July	S VI 933	1.50	3.0
A.116	26 July	H I 937	1.50	3.0
A.117	26 July	S VI 933	1.50	3.0
A.118	1 August	H I 937	1.50	3.0
A.119	1 August	S VI 933	1.50	3.0
A.120	6 August	H I 937	1.13	1.0
A.121	6 August	S VI 933	1.13	1.0
A.122	11 August	H I 937	1.50	3.0
A.123	11 August	S VI 933	1.50	3.0
A.124	14 August	H I 937	1.50	3.0
A.125	14 August	S VI 933	1.50	3.0
A.126	16 August	H I 937	1.50	3.0
A.127	16 August	S VI 933	1.50	3.0
A.128	21 August	H I 937	1.50	3.0
A.129	21 August	S VI 933	1.50	3.0
A.130	2 September	H I 937	1.50	3.0
A.131	2 September	S VI 933	1.50	3.0
A.132	6 September	H I 937	1.50	3.0
A.133	6 September	S VI 933	1.50	3.0
A.134	13 September	H I 937	1.50	3.0
A.135	13 September	S VI 933	1.50	3.0
A.136	24 September	H I 937	1.50	3.0
A.137	24 September	S VI 933	1.50	3.0
A.138	30 September	H I 937	1.50	3.0
A.139	30 September	S VI 933	1.50	3.0
A.140	5 October	H I 937	1.50	3.0
A.141	5 October	S VI 933	1.50	3.0

<sup>a</sup> Images of 24 September and later were obtained with detector B.

## 5.5 Whole-Sun Month Observations

This section of the atlas contains simultaneously recorded images in seven spectral lines and the continuum as listed in Table 5.5. The lines selected for the observations are: C I 1249  $\text{\AA}$ , Si II 1250  $\text{\AA}$ , S II 1250  $\text{\AA}$ , N V 1238  $\text{\AA}$ , O V 629  $\text{\AA}$ , Mg X 624  $\text{\AA}$ , and Fe XII 1242  $\text{\AA}$ . The continuum image was extracted from a part of the spectrum that is devoid of spectral lines near 1241  $\text{\AA}$ . The raster step size was 1.5'' in normal-step mode, and the integration time at each step was 60 s.

The images were recorded by SUMER between 10 August and 8 September 1996, and mostly represent the morphology of the disk and corona in the north-east, north-west, south-east and south-west areas of the Sun. In addition, they show the morphology of plasma structures in the vicinity of boundaries between an equatorial coronal hole (CH) and the surrounding quiet-Sun regions. The slight deformation of the limb (see, for instance, p. A.143) is caused by imperfections of the scan process.

The Whole-Sun Month study (cf. JOP 044 of *SOHO*) was designed to produce a coordinated set of observations of large-scale, stable coronal structures, such as helmet streamers and polar coronal holes. These features can persist for several rotations during solar minimum periods. Observations were acquired by the *SOHO* instruments CDS, EIT, LASCO, UVCS, and MDI, in addition to the SUMER scans shown in this atlas, and by a number of ground-based observatories.

Table 5.5: Images of coronal-hole boundaries with  $1.5'' \times 1.0''$  spatial resolution elements and 60 s integration time recorded as SUMER Whole-Sun Month observations. Images are in the lines Fe XII 1242 Å, Mg x 624 Å, O v 629 Å, N v 1238 Å (with relatively high formation temperatures), or S II 1250 Å, Si II 1250 Å, C I 1249 Å, and in the continuum at 1241 Å (with lower formation or brightness temperatures).

Atlas page	Start date 1996	Line, continuum	Area
A.142	10 August	Fe, Mg, O, N	CH northeast
A.143	10 August	S, Si, C, Cont	CH northeast
A.144	10 August	Fe, Mg, O, N	CH northwest
A.145	10 August	S, Si, C, Cont	CH northwest
A.146	11 August	Fe, Mg, O, N	CH southeast
A.147	11 August	S, Si, C, Cont	CH southeast
A.148	11 August	Fe, Mg, O, N	CH southwest
A.149	11 August	S, Si, C, Cont	CH southwest
A.150	12 August	Fe, Mg, O, N	off-limb southwest
A.151	12 August	S, Si, C, Cont	off-limb southwest
A.152	13 August	Fe, Mg, O, N	off-limb southeast
A.153	13 August	S, Si, C, Cont	off-limb southeast
A.154	15 August	Fe, Mg, O, N	off-limb northwest
A.155	15 August	S, Si, C, Cont	off-limb northwest
A.156	16 August	Fe, Mg, O, N	off-limb northeast
A.157	16 August	S, Si, C, Cont	off-limb northeast
A.158	17 August	Fe, Mg, O, N	CH northwest
A.159	17 August	S, Si, C, Cont	CH northwest
A.160	17 August	Fe, Mg, O, N	CH northeast
A.161	17 August	S, Si, C, Cont	CH northeast
A.162	18 August	Fe, Mg, O, N	CH southwest
A.163	18 August	S, Si, C, Cont	CH southwest
A.164	18 August	Fe, Mg, O, N	CH southeast
A.165	18 August	S, Si, C, Cont	CH southeast
A.166	19 August	Fe, Mg, O, N	off-limb southwest
A.167	19 August	S, Si, C, Cont	off-limb southwest
A.168	20 August	Fe, Mg, O, N	off-limb southeast
A.169	20 August	S, Si, C, Cont	off-limb southeast
A.170	21 August	Fe, Mg, O, N	off-limb northwest
A.171	21 August	S, Si, C, Cont	off-limb northwest
A.172	22 August	Fe, Mg, O, N	off-limb northeast
A.173	22 August	S, Si, C, Cont	off-limb northeast
A.174	24 August	Fe, Mg, O, N	CH northwest
A.175	24 August	S, Si, C, Cont	CH northwest
A.176	25 August	Fe, Mg, O, N	CH northeast
A.177	25 August	S, Si, C, Cont	CH northeast
A.178	25 August	Fe, Mg, O, N	CH southwest
A.179	25 August	S, Si, C, Cont	CH southwest
A.180	25 August	Fe, Mg, O, N	CH southeast
A.181	25 August	S, Si, C, Cont	CH southeast
A.182	26 August	Fe, Mg, O, N	off-limb southwest
A.183	26 August	S, Si, C, Cont	off-limb southwest
A.184	29 August	Fe, Mg, O, N	Equatorial CH
A.185	29 August	S, Si, C, Cont	Equatorial CH
A.186	30 August	Fe, Mg, O, N	Equatorial CH
A.187	30 August	S, Si, C, Cont	Equatorial CH
A.188	31 August	Fe, Mg, O, N	CH northwest
A.189	31 August	S, Si, C, Cont	CH northwest

Table 5.5: Continuation of table from previous page

Atlas page	Start date 1996	Line, continuum	Area
A.190	1 September	Fe, Mg, O, N	CH northeast
A.191	1 September	S, Si, C, Cont	CH northeast
A.192	1 September	Fe, Mg, O, N	CH southwest
A.193	1 September	S, Si, C, Cont	CH southwest
A.194	1 September	Fe, Mg, O, N	CH southeast
A.195	1 September	S, Si, C, Cont	CH southeast
A.196	4 September	Fe, Mg, O, N	CH southeast
A.197	4 September	S, Si, C, Cont	CH southeast
A.198	5 September	Fe, Mg, O, N	Streamer northwest
A.199	5 September	S, Si, C, Cont	Streamer northwest
A.200	6 September	Fe, Mg, O, N	Streamer northeast
A.201	6 September	S, Si, C, Cont	Streamer northeast
A.202	7 September	Fe, Mg, O, N	CH northwest
A.203	7 September	S, Si, C, Cont	CH northwest
A.204	8 September	Fe, Mg, O, N	CH northeast
A.205	8 September	S, Si, C, Cont	CH northeast
A.206	8 September	Fe, Mg, O, N	CH southwest
A.207	8 September	S, Si, C, Cont	CH southwest
A.208	8 September	Fe, Mg, O, N	CH southeast
A.209	8 September	S, Si, C, Cont	CH southeast

## 5.6 Equatorial Radiance Variations

Most of the solar images obtained in emission lines with formation temperatures from  $T_F \approx 1 \times 10^4$  K to  $\approx 4 \times 10^5$  K are characterized by the chromospheric network with its typical bright boundaries and dark internetwork regions. The ratio of the radiances in these regimes is of great importance for the interpretation of the transition-region plasmas. In order to provide a rough idea about this parameter, we present in Figures 5.1 and 5.2 radiances along the east-west diameter of the solar disk for emission lines and two ranges of the continuum. The radiances are shown in instrumental units, but calibration factors are provided for each observation. The diagrams also give an impression of the centre-to-limb variations and the limb brightening effects, which are very pronounced in C IV, N V, and S VI.

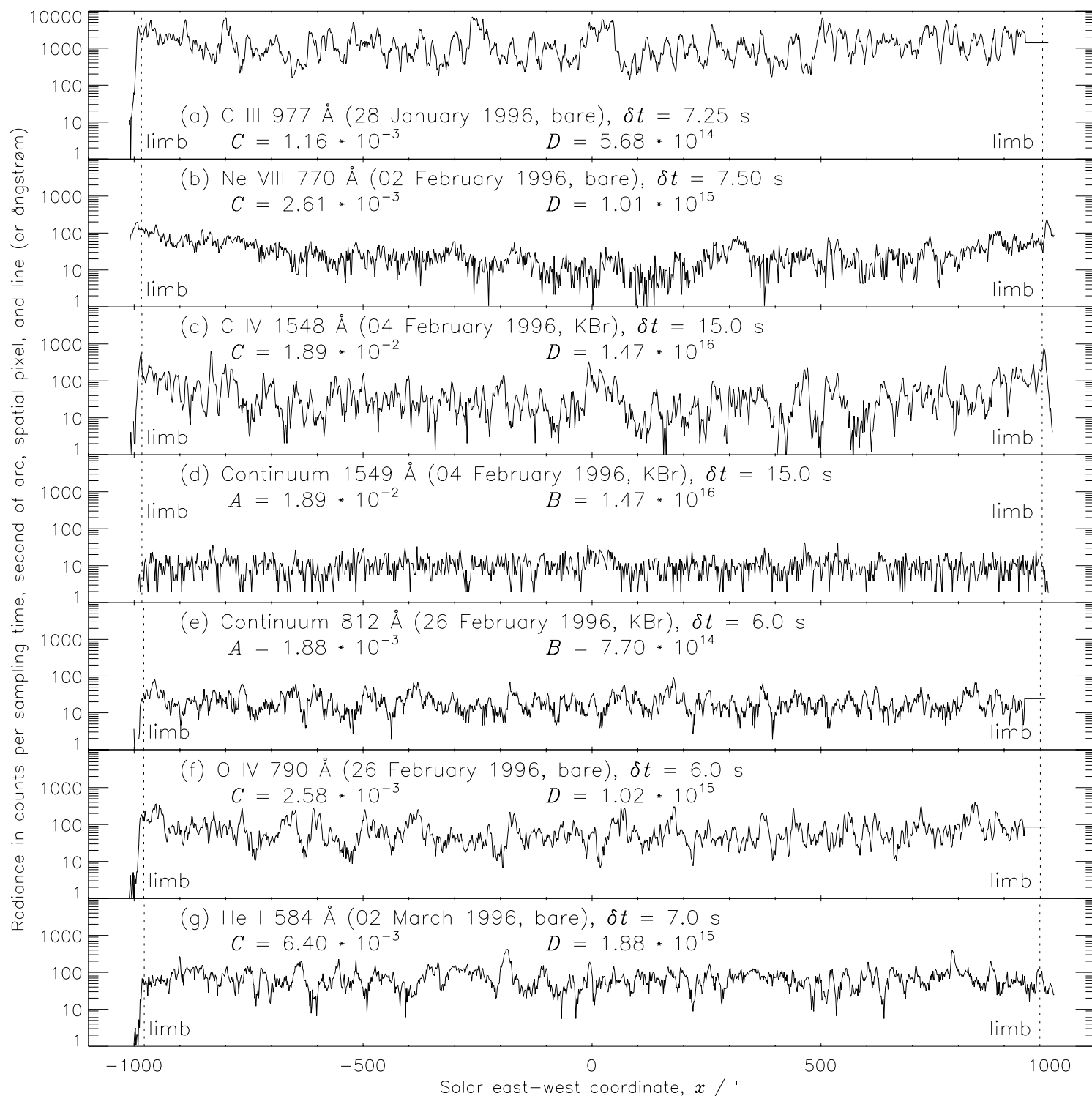


Figure 5.1: Variations of the line radiance,  $L$ , or spectral radiance,  $L_\lambda$ , across a diameter near the solar equator. (a) Radiance of the C III 977 Å line. Calibration factors:  $C$  to get  $L$  in units of  $1 \text{ W m}^{-2} \text{ sr}^{-1}$ , and  $D$  to get  $L$  in photons per second, square metre and steradian. (b) Ne VIII 770 Å line. (c) C IV 1548 Å line. (d) Spectral radiance at 1540 Å. Calibration factors:  $A$  to get  $L_\lambda$  in units of  $1 \text{ W m}^{-2} \text{ sr}^{-1} \text{ Å}^{-1}$ , and  $B$  to get  $L_\lambda$  in photons per second, square metre, steradian, and ångström. (e) Spectral radiance at 812 Å. (f) O IV 790 Å line. (g) He I 584 Å line.

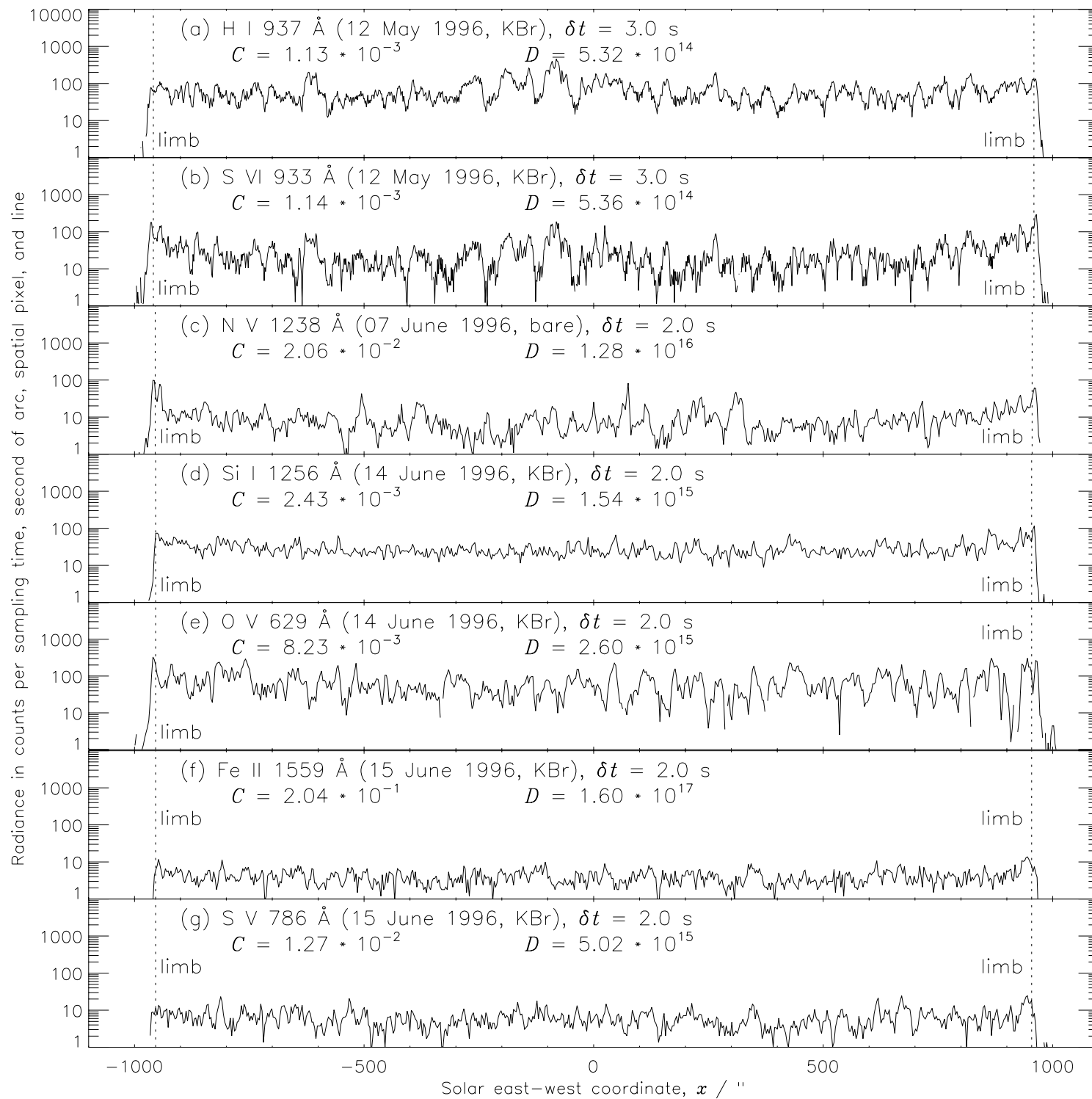


Figure 5.2: Variations of line radiance,  $L$ , across a diameter near the solar equator in the (a) H I 937 Å line, (b) S VI 933 Å line, (c) N V 1238 Å line, (d) Si I 1256 Å line, (e) O V 629 Å line, (f) Fe II 1559 Å line, and (g) S V 786 Å line. The data in panels (c) to (g) had been binned on board (see Table 5.3) and, therefore, had to be divided by a factor of three here to conform with the title of the ordinate. Calibration factors are defined according to Figure 5.1.

## 5.7 Emission-line and Spectral Irradiances

The full-Sun images can also be integrated to provide a measure of the irradiances in the observed emission lines or the spectral irradiances for certain windows of the continuum. This procedure involves complicated calculations in terms of counting-rate corrections and radiometric calibration and has been perfected over the years. We thus provide in Tables 5.6 to 5.9 the latest updates of the SUMER irradiance data. The irradiances are given for a solar distance of 1 ua (astronomical unit). A comparison with previously published values (Wilhelm et al., 1998, 1999b, 2000, 2002) reveals that both the counting rates and the calibration factors are now very stable. The high relative uncertainty estimates given for some of the lines mainly stem from the very conservative radiometric calibration uncertainties of SUMER and not from the counting-rate evaluation. A direct comparison with SOLSTICE on *UARS* showed that SOLSTICE measured in N v 1238 Å a factor of 1.14 more than SUMER, and in C iv 1548 Å a factor of 1.11 (Wilhelm et al., 1999a). With the latest SUMER calibration, we even get a factor of 1.04 for C iv (Wilhelm et al., 2002).

The continuum at 1549 Å contains a significant contribution of the H I Lyman continuum in second order. The estimate in Table 5.7 has been obtained with Figure 10.4 of Wilhelm et al. (2002).

It should be mentioned that not only the full-Sun images of SUMER have been used to calculate solar irradiances, but also the measurements made during *SOHO* roll manoeuvres, which allowed us to obtain an estimate of the centre-to-limb radiance variations of many spectral lines, too (Dammasch et al., 1999a).

Table 5.6: Irradiance,  $E$ , of emission lines from images with full spatial resolution.

Spectral line Wavelength, $\lambda/\text{\AA}$	He I 584 <sup>a</sup>	Ne VIII 770 <sup>a</sup>	O IV 790	S VI 933	H I Ly $\epsilon$ 937	S VI 944 <sup>b</sup>	C III 977	C IV 1548
Exposure time, $\delta t/s$	7.00	7.50	6.00	3.00	3.00	3.00	7.25	15.00
Angular step width, $\delta x''$	1.50	1.88	1.50	1.50	1.50	1.50	1.13	1.88
Photocathode	bare	bare	bare	KBr	KBr	KBr	bare	KBr
Spectral window in pixel <sup>c</sup>	25 (t)	25 (t)	50 (i)	50 (s)	50 (s)	50 (s)	25 (t)	50 (t)
Date in 1996	2 Mar	2 Feb	26 Feb	12 May	12 May	12 May	28 Jan	4 Feb
Solar radius from <i>SOHO</i> <sup>d</sup> , $R_{\odot}''$	978	984	979	959	959	959	984	983
Flux <sup>e</sup> , $F_{10.7}/(10^{-22} \text{ W m}^{-2} \text{ Hz}^{-1})$	69.8	74.2	70.9	75.1	75.1	75.1	71.4	71.4
Counting rate <sup>f</sup> , $N_c/(10^6 \text{ s}^{-1})$	34.42	18.65	38.35	31.53	53.81	24.18	695.6	13.83
Line irradiance, $E/(\mu\text{W m}^{-2})$	34.1	7.66	13.5	2.53	4.27	1.87	129	82.5
in photons, $E/(10^{12} \text{ s}^{-1} \text{ m}^{-2})$	10.0	2.97	5.35	1.19	2.01	0.889	63.7	64.3
Relative standard uncertainty, $u_r/\%$	16	16	17	16	15	18	18	30

<sup>a</sup>Observed in second order of diffraction.

<sup>b</sup>Blended with Si VIII (see Figure 3.3d).

<sup>c</sup>(t): spectral pixels telemetered to ground; (i): spectral pixels integrated on board; (s): estimated continuum level subtracted.

<sup>d</sup>Seen from Earth, the radius is smaller by a factor of 0.99.

<sup>e</sup>Solar Indices Bulletin (NGDC).

<sup>f</sup>Full-Sun rate.

Table 5.7: Spectral irradiance,  $E_\lambda$ , of continua from images with full spatial resolution.

Continuum wavelength, $\lambda/\text{\AA}$	804/812	1169	1549
Exposure time, $\delta t/s$	6.00	7.00	15.0
Angular step width, $\delta x/''$	1.50	1.50	1.88
Photocathode	KBr	bare	KBr
Spectral window in pixel <sup>a</sup>	50 (i)	25 (t)	50 (t)
Date in 1996	26 Feb	2 Mar	4 Feb
Solar radius from <i>SOHO</i> , $R_\odot/''$	979	978	983
Flux, $F_{10.7}/(10^{-22} \text{ W m}^{-2} \text{ Hz}^{-1})$	70.9	69.8	71.4
Counting rate <sup>b</sup> , $N_c/(10^6 \text{ s}^{-1} \text{\AA}^{-1})$	4.185	3.472	1.773 <sup>c</sup>
Spectral irradiance, $E_\lambda/(\mu\text{W m}^{-2} \text{\AA}^{-1})$	1.14	1.64	8.73 <sup>d</sup>
in photons, $E_\lambda/(10^{12} \text{ s}^{-1} \text{m}^{-2} \text{\AA}^{-1})$	0.464	0.963	6.81 <sup>d</sup>

<sup>a</sup>(t): spectral pixels telemetered to ground; (i): spectral pixels integrated on board.

<sup>b</sup>Full-Sun rate.

<sup>c</sup>The fractional contribution of the H I Lyman continuum in second order is  $\approx 20\%$ .

<sup>d</sup>Corrected for Lyman-continuum contribution.

Table 5.8: Irradiance of lines observed in first order from images with reduced spatial resolution and 50 spectral pixels integrated on board.

Spectral line Wavelength, $\lambda/\text{\AA}$	N v 1238	N v 1238	Si I 1256	Si I 1256	C IV 1548	C IV 1548	Fe II 1559
Exposure time, $\delta t/s$	2.00	2.00	2.00	2.00	2.00	2.00	2.00
Angular step width, $\delta x/''$	3.00	3.00	3.00	3.00	3.00	3.00	3.00
Photocathode	bare	bare	KBr	KBr	KBr	KBr	KBr
Date in 1996	7 Jun	14 Jun	7 Jun	14 Jun	7 Jun	16 Jun	15 Jun
Solar radius from <i>SOHO</i> , $R_\odot/''$	955	954	955	954	955	954	954
Counting rate, $N_c/(10^6 \text{ s}^{-1})$	11.64	11.33	19.40	19.10	10.37	11.93	0.883
Line irradiance, $E/(\mu\text{W m}^{-2})$	11.1	10.8	2.17	2.15	65.6	75.6	8.03
in photons, $E/(10^{12} \text{ s}^{-1} \text{m}^{-2})$	6.90	6.73	1.37	1.36	51.1	58.9	6.30

Table 5.9: Irradiance of lines observed in second order from images with reduced spatial resolution and 50 spectral pixels integrated on board.

Spectral line Wavelength, $\lambda/\text{\AA}$	He I 584	O v 629	O v 629	Ne VIII 770	Ne VIII 770	S v 786	O IV 787	O IV 787	O IV 787
Exposure time, $\delta t/s$	2.00	2.00	2.00	2.00	2.00	2.00	2.00	2.00	2.00
Angular step width, $\delta x/''$	3.00	3.00	3.00	3.00	3.00	3.00	3.00	3.00	3.00
Photocathode	bare	KBr	KBr	bare	bare	KBr	bare	KBr	bare
Date in 1996	26 Jun	07 Jun	14 Jun	07 Jun	16 Jun	15 Jun	07 Jun	15 Jun	16 Jun
Solar radius from <i>SOHO</i> , $R_\odot/''$	953	955	954	955	954	954	955	954	954
Counting rate, $N_c/(10^6 \text{ s}^{-1})$	35.66	121.5	114.3	17.98	17.71	5.142	11.38	9.005	11.10
Line irradiance, $E/(\mu\text{W m}^{-2})$	37.2	46.1	43.4	7.84	7.75	2.90	6.68	5.15	6.53
in photons, $E/(10^{12} \text{ s}^{-1} \text{m}^{-2})$	11.0	14.6	13.7	3.04	3.01	1.15	2.65	2.04	2.59

## Chapter 6

### Summary

During the first year of *SOHO* operations and later in 1999, SUMER acquired several thousand images of the solar upper atmosphere. This atlas of “Images of the Solar Upper Atmosphere from SUMER on *SOHO*” includes most of the full-Sun images that SUMER recorded and the majority of its images acquired during the Whole-Sun Month campaign. With the exception of a small number of images previously discussed in the literature (Wilhelm et al., 1997c, 1998; Hollandt et al., 1998; Wilhelm, 1999a, b; Dammasch et al., 1999c; Feldman, Widing & Warren, 1999; Wilhelm et al., 1999b; Feldman, Dammasch & Wilhelm, 2000; Wilhelm, 2000), the atlas is the first publication displaying the collection of full-Sun and Whole-Sun Month images of SUMER. Many more images depicting smaller areas of the Sun are available, but could not be included here.

One of our main tasks while selecting the atlas format has been the implementation of our desire to maintain the high spatial resolution that SUMER achieved. In particular we hope that people with average vision will be able to see the finest details of the plasma structures that SUMER can resolve. Thus the page size has been chosen such that the finest resolution element in the images corresponds to approximately  $250 \mu\text{m}$  in this atlas. For the eleven full-Sun images of the group discussed in Section 5.2, this means that individual rasters in full resolution had to be displayed in addition to the composites showing the full Sun in reduced resolution. In Section 5.5, the individual strips are also displayed in full resolution for the Whole-Sun Month. The H I 937 Å, S VI 933 Å, and S VI 944 Å images of the synoptic study were acquired with spatial resolution elements of  $1.13'' \times 1.00''$  or  $1.50'' \times 1.00''$ . In order to limit the atlas to a manageable size, we chose to present one set of the H I and S VI images in full resolution as part of the images described in Section 5.2. The remaining images of the synoptic study are displayed in reduced resolution as discussed in Section 5.4.

The images in the atlas were recorded in spectral lines or in continuum radiation emitted by plasmas spanning the electron temperature domain from  $1 \times 10^4 \text{ K}$  to  $1.4 \times 10^6 \text{ K}$ . Some of the images were recorded simultaneously in radiation emitted by plasmas of different temperatures. Due to substantial differences of the plasma properties from which the radiation originated, the atlas provides a unique source for studying many aspects of the solar upper atmosphere, just to mention a few:

- Morphologies of the plasma structures in quiet-Sun, coronal-hole and active regions.
- Morphologies of plasma structures located in interface regions between quiet-Sun, coronal-hole, and active regions.
- Differences in shapes and brightness of structures located in network boundaries and internetwork areas.
- The influence of active-region magnetic fields on neighbouring quiet-Sun and coronal-hole regions.
- Lifetimes of solar upper-atmospheric structures.
- Large-scale morphological variations in the solar upper atmosphere occurring over several solar rotations.
- Morphologies of spicules, macrospicules, filaments, and prominences.
- Morphologies and lifetimes of bright points and other small and unusually bright structures.

Not treated here are spectroscopic studies of the plasma dynamics in the solar upper atmosphere with the help of SUMER line-shift and line-broadening measurements. A complete and up-to-date list of SUMER-related publications covering all aspects that have been investigated can be found at <http://www.linmpi.mpg.de/english/projekte/sumer/text/papers.txt>.

## Bibliography

- Arnaud, M., Rothenflug, R., An Updated Evaluation of Recombination and Ionization Rates. *Astron. Astrophys. Suppl. Ser.* 60, 425–457, 1985
- Bar-Shalom, A., Klapisch, M., Oreg, J., HULLAC an Integrated Computer Package for Atomic Processes in Plasmas, *J. Quant. Spectrosc. Radiat. Transfer* 71/2-6, 169–188, 2001
- Curdt, W., Feldman, U., Laming, J.M., Wilhelm, K., Schühle, U., Lemaire, P., The Solar Disk Spectrum Between 660 and 1175 Å (First Order) Obtained by SUMER on *SOHO*, *Astron. Astrophys. Suppl. Ser.* 126, 281–296, 1997
- Curdt, W., Brekke, P., Feldman, U., Wilhelm, K., Dwivedi, B.N., Schühle, U., Lemaire, P., The SUMER Spectral Atlas of Solar-Disk Features, *Astron. Astrophys.* 375, 591–613, 2001
- Dammasch, I.E., Wilhelm, K., Curdt, W., Schühle, U., Solar Ultraviolet Irradiance and Radiance Observations by SUMER on *SOHO*, in: 9th European Meeting on Solar Physics of EPS and EAS: Magnetic Fields and Solar Processes (ed. A. Wilson), ESA SP-448, 1165–1170, 1999a
- Dammasch, I.E., Wilhelm, K., Curdt, W., Hassler, D.M., The Ne VIII ( $\lambda 770$ ) Resonance Line: Solar Wavelengths Determined by SUMER on *SOHO*, *Astron. Astrophys.* 346, 285–294, 1999b
- Dammasch, I.E., Hassler, D.M., Wilhelm, K., Curdt, W., Solar Mg X and Fe XII Wavelengths Measured by SUMER, in: Proceedings 8th *SOHO* Workshop: Plasma Dynamics and Diagnostics in the Solar Transition Region and Corona (eds. J.-C. Vial, B. Kaldeich-Schürmann), ESA SP-446, 263–268, 1999c
- Evans, J.W., Birefringent Filters, in: *The Sun* (ed. G.P. Kuiper), University of Chicago Press, Chicago, Illinois, 626–635, 1953
- Feldman, U., Behring, W.E., Curdt, W., Schühle, U., Wilhelm, K., Lemaire, P., Moran, T.M., A Coronal Spectrum in the 500–1610 Å Wavelength Range Recorded at a Height of 21 000 Kilometers Above the West Solar Limb by the SUMER Instrument on Solar and Heliospheric Observatory, *Astrophys. J. Suppl. Ser.* 113, 195–219, 1997
- Feldman, U., Widing, K.G., Warren, H.P., The Morphology of the Quiet Solar Upper Atmosphere in the  $4 \times 10^4 \leq T_e \leq 1.4 \times 10^6$  K Temperature Region, *Astrophys. J.* 522, 1133–1147, 1999
- Feldman, U., Dammasch, I.E., Wilhelm, K., The Morphology of the Solar Upper Atmosphere During the Sunspot Minimum, *Space Sci. Rev.* 93, 411–472, 2000
- Fleck, B., Domingo, V., Poland, A.I., *The SOHO Mission*, Kluwer Academic Publ., Dordrecht, Boston, London, 1995
- Fleck, B., Švestka, Z., *The First Results from SOHO*, Kluwer Academic Publ., Dordrecht, Boston, London, 1997
- Grevesse, N., Sauval, A.J., Standard Solar Composition, *Space Sci. Rev.* 85, 161–174, 1998
- Harrison, R.A., Sawyer, E.C., Carter, M.K., Cruise, A.M., Cutler, R.M., Fludra, A., Hayes, R.W., Kent, B.J., Lang, J., Parker, D.J., Payne, J., Pike, C.D., Peskett, S.C., Richards, A.G., Culhane, J.L., Norman, K., Breeveld, A.A., Breeveld, E.R., Al Janabi, K.F., McCalden, A.J., Parkinson, J.H., Self, D.G., Thomas, P.D., Poland, A.I., Thomas, R.J., Thompson, W.T., Kjeldseth-Moe, O., Brekke, P., Karud, J., Maltby, P., Aschenbach, B., Bräuninger, H., Kühne, M., Hollandt, J., Siegmund, O.H.W., Huber, M.C.E., Gabriel, A.H., Mason, H.E., Bromage, B.J.I., The Coronal Diagnostic Spectrometer for the Solar and Heliospheric Observatory, *Sol. Phys.* 162, 233–290, 1995
- Hassler, D.M., Lemaire, P., Longval, P., Polarization Sensitivity of the SUMER Instrument on *SOHO*, *Appl. Opt.* 36, 353–359, 1997

- Hassler, D.M., Dammasch, I.E., Lemaire, P., Brekke, P., Curdt, W., Mason, H.E., Vial, J.-C., Wilhelm, K., Solar Wind Outflow and the Chromospheric Magnetic Network, *Science* 283, 810–813, 1999
- Hollandt, J., Schühle, U., Paustian, W., Curdt, W., Kühne, M., Wende, B., Wilhelm, K., Radiometric Calibration of the Telescope and Ultraviolet Spectrometer SUMER on *SOHO*, *Appl. Opt.* 35, 5125–5133, 1996
- Hollandt, J., Schühle, U., Curdt, W., Dammasch, I.E., Lemaire, P., Wilhelm, K., Solar Radiometry with the Telescope and Vacuum-ultraviolet Spectrometer SUMER on the Solar and Heliospheric Observatory (*SOHO*), *Metrologia* 35, 671–675, 1998
- Kelly, R.L., Atomic and Ionic Spectrum Lines below 2000 Angstroms: Hydrogen through Krypton (Parts I to III), *J. Phys. Chem. Ref. Data* 16, 1–1678, 1987
- Landi, E., Feldman, U., Dere, K.P., CHIANTI – An Atomic Database for Emission Lines. Paper V: Comparison with an Isothermal Spectrum Observed with SUMER, *Astrophys. J. Suppl.* 139, 281–296, 2002
- Lemaire, P., Wilhelm, K., Curdt, W., Schühle, U., Marsch, E., Poland, A.I., Jordan, S.D., Thomas, R.J., Hassler, D.M., Vial, J.-C., Kühne, M., Huber, M.C.E., Siegmund, O.H.W., Gabriel, A., Timothy, J.G., Grewing, M., First Results of the SUMER Telescope and Spectrometer - Solar Ultraviolet Measurements of Emitted Radiation – on *SOHO*. (II) Imagery and Data Management, *Sol. Phys.* 170, 105–122, 1997
- Mariska, J.T., *The Solar Transition Region*, Cambridge University Press, Cambridge, 1992
- Mazzotta, P., Mazzitelli, G., Colafrancesco, S., Vittorio, N., Ionization Balance for Optically Thin Plasmas: Rate Coefficients for all Atoms and Ions of the Elements H to Ni, *Astron. Astrophys. Suppl. Ser.* 133, 403–409, 1998
- Pauluhn, A., Solanki, S.K., Schühle, U., Wilhelm, K., Lang, J., Thompson, W.T., Rüedi, I., Hollandt, J., Huber, M.C.E., Comparison of Quiet-Sun Radiances Measured by SUMER and CDS on *SOHO*, *Space Sci. Rev.* 97, 63–66, 2001a
- Pauluhn, A., Rüedi, I., Solanki, S.K., Schühle, U., Wilhelm, K., Lang, J., Thompson, W.T., Hollandt, J., Huber, M.C.E., Intercalibration of SUMER and CDS on *SOHO*. II. SUMER Detectors A and B and CDS NIS, *Appl. Opt.* 40, 6292–6300, 2001b
- Pauluhn, A., Lang, J., Schühle, U., Solanki, S.K., Wilhelm, K., Thompson, W.T., Pike, C.D., Rüedi, I., Hollandt, J., Huber, M.C.E., Intercalibration of CDS and SUMER, in: *The Radiometric Calibration of SOHO*, (eds. A. Pauluhn, M.C.E. Huber, R. v. Steiger), ISSI Scientific Report, SR-002, ISSI/ESA, 235–247, 2002
- Pettersson, J.E., The Spectrum of the Singly Ionized Sulphur, S II, *Physica Scripta* 28, 421–434, 1983
- Rottman, G.J., Woods, T.N., Sparn, T.P., Solar-Stellar Irradiance Comparison Experiment 1. 1. Instrument design and operation, *J. Geophys. Res.* 98, 10667–10677, 1993
- Rybak, J., Curdt, W., Kucera, A., Schühle, U., Wöhl, H., Chromospheric and Transition Region Dynamics – Reasons and Consequences of the Long-period Instrumental Periodicities of SUMER/*SOHO*, in: *9th European Meeting on Solar Physics of EPS and EAS: Magnetic Fields and Solar Processes* (ed. A. Wilson), ESA SP-448, 361–366, 1999
- Rybicki, G.B., Lightman, A.P., *Radiative Processes in Astrophysics*, John Wiley & Son, New York, Chichester, Brisbane, Toronto, Singapore, 1979
- Schühle, U., The Cleanliness Control Program for SUMER/*SOHO*, in: *Proceedings 10th International Colloquium on UV and X-ray Spectroscopy of Astrophysical and Laboratory Plasmas* (eds. E.H. Silver, S.M. Kahn), Cambridge University Press, Cambridge, 373–382, 1993
- Schühle, U., Brekke, P., Curdt, W., Hollandt, J., Lemaire, P., Wilhelm, K., Radiometric Calibration Tracking of the Vacuum-Ultraviolet Spectrometer SUMER During the First Year of the *SOHO* Mission, *Appl. Opt.* 37, 2646–2652, 1998
- Schühle, U., Curdt, W., Hollandt, J., Feldman, U., Lemaire, P., Wilhelm, K., Radiometric Calibration of the Vacuum-Ultraviolet Spectrograph SUMER on the *SOHO* Spacecraft with the B Detector, *Appl. Opt.* 39, 418–425, 2000

- Siegmund, O.H., Gummin, M.A., Sasseen, T., Jelinsky, P.N., Gaines, G.A., Hull, J., Stock, J.M., Edgar, M.L., Welsh, B.Y., Jelinsky, S.R., Vallergera, J.V., Microchannel Plates for the UVCS and SUMER Instruments on the *SOHO* Satellite, in: Proceedings on EUV, X-Ray, and Gamma-Ray Instrumentation for Astronomy VI (eds. O.H. Siegmund, J.V. Vallergera), SPIE 2518, 344–355, 1995
- St.Cyr, O.C., Sanchez-Duarte, L., Martens, P.C.H., Gurman, J.B., Larduinat, E., *SOHO* Ground Segment, Science Operations, and Data Products, Sol. Phys. 162, 39–59, 1995
- Thomas, R., 20:20 Vision and *SOHO* Cleanliness, in: The Radiometric Calibration of *SOHO*, (eds. A. Pauluhn, M.C.E. Huber, R. v. Steiger), ISSI Scientific Report, SR-002, ISSI/ESA, 91–104, 200
- Wadsworth, F.L.O., The Modern Spectroscope. XV., Astrophys. J. 3, 47–62, 1896
- Walker, A.B.C., Jr., Barbee, T.W., Jr., Hoover, R.B., Lindblom, J.F., Soft X-ray Images of the Solar Corona with a Normal-incidence Cassegrain Multilayer Telescope, Science 241, 1781–1787, 1988
- Wilhelm, K., The Darkest Regions of Solar Polar Coronal Holes Observed by SUMER on *SOHO*, Astrophys. Space Sci. 264, 43–52, 1999a
- Wilhelm, K., Polar Plumes: Is there a 2-Component Plasma in Coronal Holes?, in: Proceedings 8th *SOHO* Workshop: Plasma Dynamics and Diagnostics in the Solar Transition Region and Corona (eds. J.-C. Vial, B. Kaldeich-Schürmann), ESA SP-446, 707–710, 1999b
- Wilhelm, K., SUMER Observations of the Quiet Sun: Transition Region and Low Corona, Adv. Space Res. 25, 1723–1730, 2000
- Wilhelm, K., Calibration and Inter-calibration of *SOHO*'s Vacuum-ultraviolet Instrumentation, in: The Radiometric Calibration of *SOHO*, (eds. A. Pauluhn, M.C.E. Huber, R. v. Steiger), ISSI Scientific Report, SR-002, ISSI/ESA, 69–90, 2002
- Wilhelm, K., Past and Recent Observations of the Solar Upper Atmosphere at Vacuum-ultraviolet Wavelengths, J. Atmos. Sol. Terr. Phys. 65, 167–189, 2003
- Wilhelm, K., Curdt, W., Marsch, E., Schühle, U., Lemaire, P., Gabriel, A.H., Vial, J.-C., Grewing, M., Huber, M.C.E., Jordan, S.D., Poland, A.I., Thomas, R.J., Kühne, M., Timothy, J.G., Hassler, D.M., Siegmund, O.H.W., SUMER – Solar Ultraviolet Measurements of Emitted Radiation, Sol. Phys. 162, 189–231, 1995a
- Wilhelm, K., Curdt, W., Marsch, E., Schühle, U., Lemaire, P., Gabriel, A.H., Vial, J.-C., Grewing, M., Huber, M.C.E., Jordan, S.D., Poland, A.I., Thomas, R.J., Kühne, M., Timothy, J.G., Hassler, D.M., Siegmund, O.H.W., Some Design and Performance Features of SUMER: Solar Ultraviolet Measurements of Emitted Radiation, in: X-Ray and EUV/FUV Spectroscopy and Polarimetry, San Diego, CA, ed. S. Fineschi, SPIE Proc. 2517, 2–11, 1995b
- Wilhelm, K., Lemaire, P., Curdt, W., Schühle, U., Marsch, E., Poland, A.I., Jordan, S.D., Thomas, R.J., Hassler, D.M., Huber, M.C.E., Vial, J.-C., Kühne, M., Siegmund, O.H.W., Gabriel, A., Timothy, J.G., Grewing, M., Feldman, U., Hollandt, J., Brekke, P., First Results of the SUMER Telescope and Spectrometer – Solar Ultraviolet Measurements of Emitted Radiation – on *SOHO*. (I) Spectra and Spectroradiometry, Sol. Phys. 170, 75–104, 1997a
- Wilhelm, K., Lemaire, P., Feldman, U., Hollandt, J., Schühle, U., Curdt, W., Radiometric Calibration of SUMER: Refinement of the Laboratory Results Under Operational Conditions on *SOHO*, Appl. Opt. 36, 6416–6422, 1997b
- Wilhelm, K., on behalf of the SUMER Consortium, Highlights of the SUMER Observations on *SOHO*, in: Proc. 5th *SOHO* Workshop: The Corona and Solar Wind Near Minimum Activity (ed. A. Wilson), ESA SP-404, 17–28, 1997c
- Wilhelm, K., Lemaire, P., Dammasch, I.E., Hollandt, J., Schühle, U., Curdt, W., Kucera, T., Hassler, D.M., Huber, M.C.E., Solar Irradiances and Radiances of UV and EUV Lines During the Minimum of the Sunspot Activity in 1996, Astron. Astrophys. 334, 685–702, 1998
- Wilhelm, K., Woods, T.N., Schühle, U., Curdt, W., Lemaire, P., Rottman, G.J., The solar ultraviolet spectrum from 1200 Å to 1560 Å: A Radiometric Comparison between SUMER/*SOHO* and SOLSTICE/*UARS*, Astron. Astrophys. 352, 321–326, 1999a

Wilhelm, K., Lemaire, P., Dammasch, I.E., Hollandt, J., Schühle, U., Curdt, W., Kucera, T., Hassler, D.M., Huber, M.C.E., Solar Irradiances of UV and EUV Lines During the Minimum of the Sunspot Activity in 1996, *Adv. Space Res.* 24, 229–232, 1999b

Wilhelm, K., Schühle, U., Curdt, W., Dammasch, I.E., Hollandt, J., Lemaire, P., Huber, M.C.E., Solar Spectroradiometry with the Telescope and Spectrograph SUMER on the Solar and Heliospheric Observatory *SOHO*, *Metrologia* 37, 393–398, 2000

Wilhelm, K., Schühle, U., Curdt, W., Dammasch, I.E., Hollandt, J., Lemaire, P., Huber, M.C.E., Solar Vacuum-ultraviolet Radiometry with SUMER, in: *The Radiometric Calibration of SOHO*, (eds. A. Pauluhn, M.C.E. Huber, R. v. Steiger), ISSI Scientific Report, SR-002, ISSI/ESA, 145–160, 2002

Zirin, H., *The Solar Atmosphere*, Blaisdell Publishing Co., Waltham, Toronto, London, 1966